OPTICAL CHARACTERIZATION OF THERMAL TRANSPORT IN MULTIFUNCTIONAL MATERIALS

BY

AKASH RAI

THESIS

Submitted in partial fulfillment of the requirements
for the degree of Master of Science in Materials Science and Engineering
in the Graduate College of the
University of Illinois Urbana-Champaign, 2021

Urbana, Illinois

Adviser:

Professor David G. Cahill

ABSTRACT

Understanding thermal transport properties of materials is essential for both device applications and materials physics. Thermal conductivity and interface thermal conductance are fundamental materials properties and important engineering parameters for small-scale device applications. In addition, the effect of isotopic mass disorder on the vibrational properties of ultrahigh thermal conductivity material becomes important with significantly reduced anharmonicity and the improvements in the quality of crystal growth.

In this thesis, I use ultrafast pump-probe laser based optical characterization technique to experimentally investigate anisotropic thermal transport properties of layered InSe that is recently prepared in two-dimensional (2D) structures and have distinct in-plane anisotropies. InSe is a promising candidate for next-generation electronics and optoelectronics, owing to its high electron mobility and direct optical bandgap in the few-layer limit. The knowledge of thermal transport properties is needed for engineering heat dissipation in devices. I report the room-temperature thermal conductivity of exfoliated crystals of InSe along the through-plane and in-plane directions using conventional and beam offset time domain thermoreflectance (TDTR), respectively.

InSe crystals with varying thicknesses were prepared by mechanical exfoliation onto Si(100) wafers followed by immediate encapsulation with a 3-nm-thick AlO_x passivation layer to prevent ambient degradation prior to coating with metal films for TDTR measurements. The measured thermal conductivity in the in-plane direction, $\Lambda_{in} \approx 8.5 \pm 2$ W/m-K, is an order of magnitude higher than that in the through-plane direction, $\Lambda_{through} \approx 0.76 \pm 0.15$ W/m-K, which implies a high thermal anisotropy $\approx 11 \pm 3$. This relatively high anisotropy and low thermal

conductivity compared to other layered semiconductors imply that InSe will require unique thermal management considerations when implemented in electronic, optoelectronic, and thermoelectric applications.

The second topic I investigate is the effect of isotopic disorder on the vibrational properties of cubic boron arsenide (*c*-BAs) at room temperature using Raman spectroscopy. Boron arsenide is at the forefront of research on ultrahigh thermal conductivity materials. I report a Raman scattering study of isotopically tailored cubic boron arsenide single crystals for 11 isotopic compositions spanning the range from nearly pure *c*-^{10}BAs to nearly pure *c*-^{11}BAs. The results provide insights on the effects of strong mass disorder on optical phonons and the appearance of two-mode behavior in the Raman spectra of mixed crystals, not seen before in isotopically disordered materials. Strong isotope disorder also relaxes the one-phonon Raman selection rules, resulting in disorder activated Raman scattering by acoustic and optical phonons.

ACKNOWLEDGMENTS

I owe a debt of gratitude to many people in graduate school. First on the list is my advisor, Prof. David G. Cahill, for his guidance over the course of my master's degree. His knowledge and drive are inspirational, as is his dedication to scientific research. I really admire his critical thinking and methodical problem-solving approach. Prof. Cahill displayed a lot of patience and understanding during my master's research, a time in which I struggled with experimental challenges and produced no significant results for long time. He pushed me to achieve more than I realized I was capable of and supported me at every step of my research. Working with him has improved my approach in experimentation as well as scientific communications, and his style of working will keep inspiring me in future career.

It has been my privilege to work with such smart and motivated people in UIUC. I thank my fellow group members and alumni, Qiye, Jungwoo, Ella, Kexin, Sushant, Renee, Kisung, Guangxin, and Xiaoyang. I would like to give special thanks to Hyejin Jang for helping me with getting started in the group and building a solid background in TDTR, and Zhu Diao for his hand-on help. I thank Darshan Chalise for our friendship and numerous discussions we had for last two years. I also acknowledge the support from excellent staffs in the Materials Research Laboratory and my collaborators.

Finally, I am deeply grateful for my family for their endless support and love at every point of the graduate school.

I acknowledge financial support from National Science Foundation Grant No. EFRI-1433467, and Office of Naval Research (ONR) under MURI Grant No. N00014-16-1-2436.

TABLE OF CONTENTS

CHAPTER 1

INTRODUCTION

1.1 Motivation

Heat transfer, including conduction, convection, and radiation, is one of the fundamental energy transport mechanisms in nature [1-3]. Thermal conductivity (Λ) is the property of a material to conduct heat and is an important intrinsic material property. Interface conductance (G) is the radiative heat transfer property of interface. Both thermal conductivity and interface conductance are critical parameters in various engineering systems [1,3,4]. In different engineering system, the demand for the functional materials for thermal management varies greatly.

Understanding thermal transport properties of materials is essential for engineering of small-scale devices. Heat dissipation in high power density devices is the bottleneck for semiconductor industries trying to reach miniaturization of devices [5]. Non uniform power distribution in these microelectronic devices results in concentrated heat sources with extremely high heat flux ~1 kW/cm^2 [6,7]. Proper cooling of heat should be provided through electrical contacts and requires the knowledge of thermal conductivity of constituent materials and interfacial thermal transport between different materials. Discovering high thermal conductivity (κ) materials to enable efficient heat dissipation from hot spots are imperative for thermal management in next generation electronic and optoelectronic devices [8,9]. Recent innovations also require the development of materials with high thermal conduction anisotropy, which can remove hotspots along the fast-axis direction and provide thermal insulation along the slow axis [10,11].

In this thesis, I study thermal transport properties of various materials systems using ultrafast pump-probe based characterization techniques and Raman spectroscopy. I determine equilibrium anisotropic thermal transport properties of layered InSe flakes that were recently prepared in two-dimensional (2D) structures and have distinct in-plane anisotropies (Chap. 3). I also investigate the effect of isotopic disorder on the vibrational properties of cubic boron arsenide (Chap. 4) using Raman spectroscopy.

1.2 Two-dimensional materials with distinct in-plane anisotropy

Van der Waals layered materials have attracted great interest for next-generation electronics and optoelectronic materials due to their high charge carrier mobilities, diverse band structures, large oscillator strengths, unprecedented tunability, and access to novel spin and valley degrees of freedom [12-16]. Due to the anisotropic atomic bonding structure, i.e., strong covalent bonds within the planes and much weaker van der Waals bonds along the layering axis, the layered materials can be easily isolated into atomically thin but stable structures consisting of only one or few layers. The low dimensionality gives rise to novel and exotic materials behaviors. For example, the exceptionally high carrier mobilities on the planes and tunable electron band gaps make 2D materials promising for transistors and optoelectronic devices of nanoscale [17]. Weak inter-layer van der Waals bonding not only allows isolation of monolayers and few-layer crystals through exfoliation but also enables diverse van der Waals heterojunctions through stacking assembly [12,18,19].

Among layered semiconductors, transition metal dichalcogenides (TMDCs) have received significant attention for device applications due to their strong layer dependence, large exciton binding energies, and successful wafer-scale growth [13,20,21]. However, most TMDC

semiconductors only possess a direct bandgap in the monolayer limit, which hinders the utilization of thicker films that are optimal for optoelectronics applications. On the other hand, post-transition metal chalcogenide (PTMC) semiconductors not only possess a direct bandgap in multi-layer films but also possess higher charge carrier mobilities than TMDCs [12,22].

Among the PTMCs, layered indium selenide (InSe) is among the most promising n-type semiconductors because of its high electron mobility (>1000 cm^2/V-s) at room temperature [22,23]. Furthermore, InSe has a direct bandgap at all beyond-monolayer thicknesses, which is desired for many photodetector and photovoltaic applications [22]. For example, with a bandgap of 1.25 eV that approaches the ideal Shockley-Queisser limit (i.e., 1.34 eV) and a low surface recombination velocity ($\approx 4 \times 10^4$ cm s^{-1}), multi-layer InSe is ideal for ultra-compact photovoltaics [22, 24-27]. InSe phototransistors also show a high photoresponsivity ($\approx 10^7$ A/W at 514 nm) and a ballistic avalanche photo response when paired with p-type black phosphorus [28-30]. Few-layer InSe has further shown promise for heterogeneous catalysis, spintronic devices, and thermoelectric energy conversion [31-34]. Specifically, the band dispersion of InSe results in a high Seebeck coefficient that enhances the thermoelectric figure of merit (ZT) [34].

The realization of these InSe device concepts in scaled systems will require high-density integration with effective thermal management. Therefore, quantification of the thermal conductivity for exfoliated InSe in both the in-plane and through-plane directions is paramount for future application development. For example, the optimal design of low-noise InSe photodetectors and high-gain InSe avalanche photodiodes will require a detailed understanding of electron-phonon coupling and hot carrier dynamics [25,29,35]. Moreover, ultracompact InSe photovoltaic cells will rely on effective heat dissipation strategies, especially in solar concentration schemes [26]. However, there are limited experimental studies of the intrinsic

thermal properties of bulk InSe crystals and no reports on exfoliated InSe flakes[36-38]. Thermal transport measurements of InSe in ambient conditions possess a technical challenge due to the high chemical reactivity of InSe that results in rapid oxidation and significant degradation of intrinsic properties[40]. To circumvent this issue, seeded atomic layer deposition of an alumina encapsulation layer on exfoliated InSe flakes is employed to impart ambient stability during TDTR measurements.

In this study, I use conventional [41] and beam-offset [42,43] time-domain thermoreflectance (TDTR), which account for through-plane and in-plane thermal transport, respectively. From measurements, I derive the 3D thermal conductivity tensors of InSe, along the three coordination axes. The in-plane thermal conductivity is higher than the through-plane thermal conductivity by more than an order of magnitude, due to the layered structures. The variation of both in-plane and through-plane conductivity with thickness of sample is discussed.

1.3 Effect of isotope disorder in binary semiconductors

Discovering high thermal conductivity (κ) materials to enable efficient heat dissipation from hot spots are imperative for thermal management in next generation electronic and optoelectronic devices. After decades of efforts, only few non-metallic materials have been found to show high thermal conductivity (κ) > 400 W/m-K (κ of Cu) at room temperature (RT) [44]. Highest thermal conductivity is measured for diamond, reaching about 2200 W/m-K at room temperature [44,45,46]. However, the high cost and slow synthesis to produce high quality, single crystal diamond on wafer scale makes it ineffective to be used as heat dissipator in electronic devices. Besides diamond, a set of non-metallic crystals with high κ were systematically identified by Slack in 1973 including silicon carbide (SiC), boron phosphide (BP)

and cubic boron nitride (c-BN) based on an approximate model that captured the need for high group velocity and low phonon scattering rates [47,48,49]. This model suggested the candidates for high κ materials should conventionally have low average atomic mass of the constituent elements, having stiff bonding in a simple atomic structure with low anharmonicity. Based on this widely accepted theory, for decades cubic boron arsenide (*c*-BAs) was expected to have an unremarkable κ of about 200 W/m-K, although this value was never measured [47].

In 2013, Lindsay, Broido, and Reinecke did first principle calculations on the thermal transport properties of boron based cubic III-V compounds and predicted that the conventional criteria for high κ materials are incomplete and pointed to new ones stemming from fundamental vibrational properties [50]. They calculated a remarkable room temperature (RT) thermal conductivity (κ) for *c*-BAs of about 2200 W/m-K comparable to that of diamond and graphite considering lowest order anharmonicity [50]. They attributed this high RT κ in *c*-BAs to its unusual vibrational properties that results in significantly reduced three-phonon scattering due to a large frequency gap between its acoustic and optical phonons (a-o gap) and bunching of the acoustic phonon dispersions branch [50].

A more recent study on higher-order anharmonicity found a surprisingly high four-phonon scattering in *c*-BAs, reducing its predicted κ from 2200 W/m-K to about 1400 W/m-K at room temperature [51]. Navaneetha *et al.* also calculated the effect of higher order anharmonicity in phonon dynamics of strongly bonded solids [52]. They identified new selection rules on three-phonon processes, that are dictated entirely by features in the phonon dispersions and are critical for new trends to be identified to aid in the search for materials with high κ in the zinc blende compounds. Various experimental groups have synthesized high quality bulk *c*-BAs single crystals, with natural isotopic compositions of boron, and measured its room temperature κ value

to be around 900-1300 W/m-K [53,54,55], very close to the calculated value considering higher order anharmonicity.

This difference in the measured κ value from the predicted value is attributed to extrinsic defects in the *c*-BAs such as isotopic disorder, impurity, and dislocations. As the quality of grown single crystals improves, the enhancement in RT κ of *c*-BAs depends on the reduction in phonon-isotope scattering, which is simplest manifestation of substitutional disorder in crystal. A first principle calculation on phonon-isotope scattering by Lindsay *et al.* predicted a significant enhancement in the RT κ value (~50%) in isotopically pure *c*-BAs compared to that with natural isotopic compositions [56]. They also examined many materials with significant isotope effect, an enhancement in their RT κ value with isotopic purification [56]. Thus, the effect of isotopic disorder on the vibrational properties of *c*-BAs becomes significant in accurately predicting the thermal transport properties.

1.3.1 Coherent Potential Approximation

Raman scattering has been a method of choice to experimentally investigate isotopic disorder effects in on phonons and understand the fundamental vibrational properties of a material [57,58]. For an ideal crystal within harmonic approximation, the reduced mass (μ) dependence of Raman shift (ν) associated with zone center optical phonon peak follows:

$$\nu \propto \mu^{-1/2} \tag{1.1}$$

In real crystals, this ideal mass scaling law fails due to isotopic disorder and anharmonicity that gives rise to an additional complex phonon self-energy Σ(ν),

$$\Sigma(\nu) \approx \Sigma_{dis}(\nu) + \Sigma_{anh}(\nu) \tag{1.2}$$

Here, $\Sigma_{dis}(\nu)$ and $\Sigma_{anh}(\nu)$ is the complex phonon self-energy arising due to isotopic disorder and anharmonicity respectively [58]. $\Sigma_{dis}(\nu)$ can be decomposed into the real part and imaginary part,

$$\Sigma_{dis}(\nu) = \Delta_{dis}(\nu) - i\Gamma_{dis}(\nu) \quad (1.3)$$

here, $\Delta_{dis}(\nu)$ can be directly related to the phonon frequency shift due to presence of isotopic disorder [58].

If the anharmonicity is assumed to be approximately same for all the isotopic compositions, then the deviation of the measured Raman shift for each composition from its expected value under ideal mass scaling law from equation (1) can be used to quantify Δ_{dis}. Phonons in an ideal crystal have infinite lifetime under harmonic approximation. In real crystal with no isotopic disorder, the phonon lifetime becomes finite due to anharmonicity and the phonon lineshape is Lorentzian. This phonon lineshape is distorted in the presence of isotopic disorder. The spectral band-broadening in isotopically impure crystals relative to isotopically enriched sample be directly related to $\Gamma_{dis}(\nu)$. A theoretical investigation for the phonon self-energy due isotope effect was done in previous studies [57,58,59,60,61] using lowest order perturbation theory and coherent potential approximation (CPA).

Recently Mahan did some theoretical calculations to derive the effect of atomic isotopes on the phonon modes of a crystal and investigated the influence of atomic isotopes on the dispersion of the phonons. He used green's function approach to derive the formula for the change in the phonon dispersion in bulk three-dimensional crystals and concluded that in solving for the vibrational modes, the mixing of modes caused by isotope scattering is an important process [62]. Similar work was done by Pettes *et al.* where they invoke the virtual crystal approximation in a treatment of graphite thin films, to discuss the changes in the phonon dispersion caused by scattering from isotope variations [63].

The vibrational properties of cubic boron arsenide with natural isotope abundance (^{nat}BAs) and cubic boron arsenide isotopically enriched with ^{11}B (^{11}BAs) were studied by Hadjiev *et al.* using Raman spectroscopy and first-principles density functional perturbation theory (DFPT) [61]. In ^{nat}BAs, they observed an anomalous two-mode behavior not seen in other isotopically disordered crystals; they tentatively attributed this behavior to the localization of ^{10}B vibrational states. They also observed a lack of LO-TO splitting in the measured Raman spectrum of ^{11}BAs and further investigated the small LO-TO splitting in ^{nat}BAs using DFPT [61]. The calculated phonon dispersion of *c*-BAs includes overbending of the upmost optical phonon branch [61]; i.e., the frequency of phonons on the non-degenerate optical branch is higher than that of the zone-center phonon, like the optical phonon dispersion of diamond [64]. They evaluated the real part of phonon self-energy in ^{nat}BAs arising due to isotopic disorder at zone center as $\Delta_{dis} \approx -3$ cm^{-1}, with small disorder-induced broadening $\Gamma_{dis} \approx 0.4$ cm^{-1} [61].

1.3.2 Two-mode behavior in mixed crystals

The two-mode behavior seen in the Raman spectra of ^{nat}BAs is often observed in mixed crystals of the type $LM_{1-x}N_x$, where the Raman frequencies of the LM and LN components differ significantly [65,69]. At any intermediate compositions *x*, two sets of frequencies are often observed; one set of frequencies is related to the LO and TO modes of the lighter LM component, and the other set of frequencies is related to the LO and TO modes of the heavier LN component [69]. There have been numerous attempts to provide a theoretical criterion for predicting one-or two-mode behavior in mixed diatomic crystal. These criteria are extensively reviewed by Sen and Hartmann [67].

Chang and Mitra proposed a modified-random-element-isodisplacement (MREI) model that assumed that all cation-anion pairs vibrate in phase, as in the $k = 0$ optic mode of a perfect diatomic crystal [65]. This leads to a criterion for two-mode behavior depending only on the masses of constituents,

$$m_M^{-1} > m_I^{-1} + m_N^{-1} \tag{1.4}$$

here, $\mu_{I,N}^{-1} = m_I^{-1} + m_N^{-1}$ is the reduced mass of the compound LN.

This criterion states that a mixed crystal that displays two-mode behavior has a substituting atom with a mass smaller than the reduced mass of the compound formed by the other two atoms. They successfully applied this criterion to predict one- and two-mode behavior in various mixed crystals [65]. Figure 1.1 shows the summary of this condition tested on mixed crystals by Chang and Mitra together with c-$^{10}B_{1-x}{}^{11}B_xAs$, i.e., a ^{10}B impurity in ^{11}BAs. The dashed line represents the condition stated in Eq. 1.4 and forms a separating boundary between one- and two-mode behavior in mixed crystals. As seen in Figure 1.1, *c*-BAs lies almost exactly on the dashed line and is therefore at the cusp of satisfying this condition of two-mode behavior.

In this study I use Raman spectroscopy to investigate the vibrational properties of isotopically tailored cubic boron arsenide single crystals at room temperature that aim to provide more comprehensive picture of the isotope effects in these disordered *c*-BAs single crystals. A clear understanding of this isotopic disorder effect on the vibrational properties along with the ongoing research on the effect higher order anharmonicity and will complement the computational groups to predict the criteria to find ultrahigh κ materials. While some of these isotopic compositions (^{11}BAs, ^{nat}BAs, $^{10}B_{0.5}{}^{11}B_{0.5}As$ and ^{10}BAs) have been experimentally investigated recently using Raman spectroscopy [61], they are not sufficient to understand and predict the self-energy aspect arising due to this isotopic disorder. The availability of various

high purity isotopic compositions of c-$^{10}B_x{}^{11}B_{1-x}As$ single crystals have made it possible to study the phonon dynamics of zinc blend *c*-BAs single crystals with varying isotopic disorder and reveal the anomalous two-mode behavior.

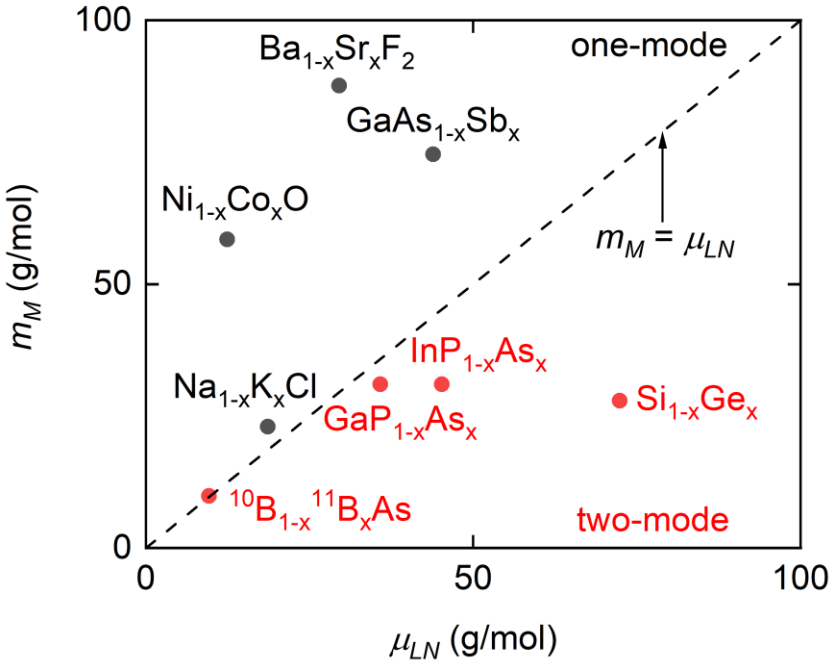

Figure 1.1. Summary of the two-mode behavior criterion [Eq. (1.4)] proposed by Chang and Mitra,[65] tested on selected mixed crystals of the type $LM_{1-x}N_x$ (mixture of the compound LM and the compound LN) along with *c*-$^{10}B_{1-x}{}^{11}B_xAs$ (^{10}B substituting in ^{11}BAs). The *y* axis is the mass of the substituting element M (m_M) and the x axis is the reduced mass (μ_{LN}) of the compound LN. One-mode behavior mixed crystals: *LN*-arbitrary binary compound with element *L* (O, Cl, Ga, F_2) and *N* (K, Co, Sr, Sb). *LM*-arbitrary binary compound with element *L* (O, Cl, Ga, F_2) and *M* (N, Ni, Ba, As). The dashed line represents the condition $m_M = \mu_{LN}$ and forms a separating boundary between one- and two-mode crystals. The behavior of mixed crystals is drawn from Refs. [65].

1.4 References

1. C. Kittel, *Introduction to solid state physics* (Wiley, 1986).
2. G. Chen, *Nanoscale Energy Transport and Conversion: A Parallel Treatment of Electrons, Molecules, Phonons, and Photons* (Oxford University Press, 2005).
3. A. F. Mills, *Heat Transfer* (Prentice Hall, 1999).
4. J. M. Ziman, *Electrons and Phonons: The Theory of Transport Phenomena in Solids* (OUP Oxford, 1960).
5. D. G. Cahill, P. V Braun, G. Chen, D. R. Clarke, S. Fan, K. E. Goodson, P. Keblinski, W. P. King, G. D. Mahan, A. Majumdar, H. J. Maris, S. R. Phillpot, E. Pop, and L. Shi, *Appl. Phys. Rev.* **1**, 11305 (2014).
6. M. M. Waldrop, Nature 530, 144 (2016).
7. S. V. Garimella, A. S. Fleischer, J. Y. Murthy, A. Keshavarzi, R. Prasher, C. Patel, S. H. Bhavnani, R. Venkatasubramanian, R. Mahajan, Y. Joshi, B. Sammakia, B. A. Myers, L. Chorosinski, M. Baelmans, P. Sathyamurthy, and P. E. Raad, IEEE Trans. Compon. Packag. Technol., 31, 801 (2008).
8. Y. Cui, M. Li, and Y. Hu, J. Mater. Chem. C 8, 10568–10586 (2020).
9. A. L. Moore and L. Shi, Mater. Today 17, 163–174 (2014).
10. J. Norley, J. J. Tzeng, G. Getz, J. Klug, and B. Fedor, In Seventeenth Annual IEEE Semiconductor Thermal Measurement and Management Symposium 107–110 (IEEE, 2001).
11. D. D. L. Chung and Y. Takizawa, J. Electron. Mater. 41, 2580–2587 (2012).
12. V. K. Sangwan and M. C. Hersam, Annu. Rev. Phys. Chem. 69, 299 (2018).
13. D. Jariwala, V. K. Sangwan, L. J. Lauhon, T. J. Marks, and M. C. Hersam, ACS Nano 8, 1102 (2014).
14. J. R. Schaibley, H. Yu, G. Clark, P. Rivera, J. S. Ross, K. L. Seyler, W. Yao, and X. Xu, Nat. Rev. Mater. 1, 16055 (2016).
15. I. Choudhuri, P. Bhauriyal, and B. Pathak, Chem. Mater. 31, 8260 (2019).
16. M. Gibertini, M. Koperski, A. F. Morpurgo, and K. S. Novoselov, Nat. Nanotechnol. 14, 408 (2019).
17. P. M. Ajayan, P. Kim, and K. Banerjee, Phys. Today 69, 38 (2016).
18. D. Jariwala, T. J. Marks, and M. C. Hersam, Nat. Mater. 16, 170 (2017).
19. Y. Liu, Y. Huang, and X. Duan, Nature 567, 323 (2019).
20. K. Kang, S. Xie, L. Huang, Y. Han, P. Y. Huang, K. F. Mak, C.-J. Kim, D. Muller, and J. Park, Nature 520, 656 (2015).
21. Q. H. Wang, K. Kalantar-Zadeh, A. Kis, J. N. Coleman, and M. S. Strano, Nat. Nanotechnol. 7, 699 (2012).
22. D. A. Bandurin, A. V. Tyurnina, G. L. Yu, A. Mishchenko, V. Zolyomi, S. V. Morozov, R. K. Kumar, R. V. Gorbachev, Z. R. Kudrynskyi, S. Pezzini, Z. D. Kovalyuk, U. Zeitler, K. S. Novoselov, A. Patane`, L. Eaves, I. V. Grigorieva, V. I. Fal'Ko, A. K. Geim, and Y. Cao, Nat. Nanotechnol. 12, 223 (2017).
23. M. Li, C.-Y. Lin, S.-H. Yang, Y.-M. Chang, J.-K. Chang, F.-S. Yang, C. Zhong, W.-B. Jian, C.-H. Lien, C.-H. Ho, H.-J. Liu, R. Huang, W. Li, Y.-F. Lin, and J. Chu, Adv. Mater. 30, 1803690 (2018).
24. A. Segura, J. P. Guesdon, J.M. Besson, andA.Chevy, J. Appl. Phys. 54, 876 (1983).
25. C. Zhong, V. K. Sangwan, J. Kang, J. Luxa, Z. Sofer, M. C. Hersam, and E. A. Weiss, J. Phys. Chem. Lett. 10, 493 (2019).

26. D. Jariwala, A. R. Davoyan, J. Wong, and H. A. Atwater, ACS Photonics 4, 2962 (2017).
27. H. Bergeron, L. M. Guiney, M. E. Beck, C. Zhang, V. K. Sangwan, C. G. Torres-Castanedo, J. T. Gish, R. Rao, D. R. Austin, S. Guo, D. Lam, K. Su, P. T. Brown, N. R. Glavin, B. Maruyama, M. J. Bedzyk, V. P. Dravid, and M. C. Hersam, Appl. Phys. Rev. 7, 041402 (2020).
28. J. Kang, S. A. Wells, V. K. Sangwan, D. Lam, X. Liu, J. Luxa, Z. Sofer, and M. C. Hersam, Adv. Mater. 30, 1802990 (2018).
29. A. Gao, J. Lai, Y. Wang, Z. Zhu, J. Zeng, G. Yu, N. Wang, W. Chen, T. Cao, W. Hu, D. Sun, X. Chen, F. Miao, Y. Shi, and X. Wang, Nat. Nanotechnol. 14, 217 (2019).
30. S. D. Lei, L. H. Ge, S. Najmaei, A. George, R. Kappera, J. Lou, M. Chhowalla, H. Yamaguchi, G. Gupta, R. Vajtai, A. D. Mohite, and P. M. Ajayan, ACS Nano 8,1263 (2014).
31. E. Petroni, E. Lago, S. Bellani, D. W. Boukhvalov, A. Politano, B. G€urbulak, S. Duman, M. Prato, S. Gentiluomo, R. Oropesa-Nu~nez, J.-K. Panda, P. S. Toth, A. E. Del Rio Castillo, V. Pellegrini, and F. Bonaccorso, Small 14, 1800749 (2018).
32. K. Premasiri, S. K. Radha, S. Sucharitakul, U. R. Kumar, R. Sankar, F.-C. Chou, Y.-T. Chen, and X. P. A. Gao, Nano Lett. 18, 4403 (2018).
33. N. T. Hung, A. R. T. Nugraha, and R. Saito, Appl. Phys. Lett. 111, 092107 (2017).
34. D. Wickramaratne, F. Zahid, and R. K. Lake, J. Appl. Phys. 118, 075101 (2015).
35. S. Lei, F. Wen, L. Ge, S. Najmaei, A. George, Y. Gong, W. Gao, Z. Jin, B. Li, J. Lou, J. Kono, R. Vajtai, P. Ajayan, and N. J. Halas, Nano Lett. 15, 3048 (2015).
36. A. V. Tyurin, K. S. Gavrichev, and V. P. Zlomanov, Inorg. Mater. 43, 921 (2007).
37. D. P. Spitzer, J. Phys. Chem. Solids 31, 19 (1970).
38. G. D. Guseinov, A. I. Rasulov, E. M. Kerimova, and M. Z. Ismailov, Phys. Status Solidi B 19, K7 (1967).
39. A. Shafique and Y.-H. Shin, Sci. Rep. 10, 1093 (2020).
40. S. A. Wells, A. Henning, J. T. Gish, V. K. Sangwan, L. J. Lauhon, and M. C. Hersam, Nano Lett. 18, 7876 (2018).
41. D. G. Cahill, *Rev. Sci. Instrum.* **75**, 5119 (2004).
42. J. P. Feser and D. G. Cahill, *Rev. Sci. Instrum.* **83**, 104901 (2012).
43. J. P. Feser, J. Liu, and D. G. Cahill, *Rev. Sci. Instrum.* **85**, 104903 (2014).
44. C. Dames, Science 361, 549 (2018).
45. J. R. Olson, R. O. Pohl, J. W. Vandersande, A. Zoltan, T. R. Anthony, and W. F. Banholzer, Phys. Rev. B 47, 14850 (1993).
46. L. Wei, P. K. Kuo, R. L. Thomas, T. R. Anthony, and W. F. Banholzer Phys. Rev. Lett. 70, 3764 (1993).
47. G. A. Slack, J. Phys. Chem. Solids 34, 321–335 (1973).
48. R. H. Wentorf, Jr. J. Chem. Phys. 26, 956 (1957).
49. G. A. Slack, J. Appl. Phys. 35 (12) 3460-3466 (1964).
50. L. Lindsay, D. A. Broido, and T. L. Reinecke, Phys. Rev. Lett. 111, 025901 (2013).
51. T. Feng, L. Lindsay, and X. Ruan, Physical Review B 96, 161201 (2017).
52. N.K. Ravichandran and D. A. Broido, "Phonon-Phonon Interactions in Strongly Bonded Solids: Selection Rules and Higher-Order Processes", submitted for publication (2020).
53. J. S. Kang, M. Li, H. Wu, H. Nguyen, Y. Hu, Science 361, 575-578 (2018).
54. S. Li, Q. Zheng, Y. Lv, X. Liu, X. Wang, P.Y. Huang, D. G. Cahill, B. Lv, Science 361, 579-581 (2018).
55. F. Tian, B. Song, X. Chen, N.K. Ravichandran, Y. Lv, *et al.* Science 361, 582-585 (2018).

56. L. Lindsay, D. A. Broido, and T. L. Reinecke, Phys. Rev. B 88, 144306 (2013).
57. F. Widulle, T. Ruf, M. Konuma, I. Silier, M. Cardona, W. Kriegseis, and V. Ozhogin, Solid State Communications 118, 1 (2001).
58. M. Cardona and T. Ruf, Solid State Communications 117, 201 (2001).
59. S.-I. Tamura, Physical Review B 27, 858 (1983).
60. S.-I. Tamura, Physical Review B 30, 849 (1984).
61. V.G. Hadjiev, M.N. Iliev, B. Lv, Z.F. Ren, and C.W. Chu, Physical Review B 89, (2014).
62. G. D. Mahan, Phys. Rev. B 100, 024307 (2019).
63. M. T. Pettes, M. M. Sadeghi, H. Ji, I. Jo,W.Wu, R. S. Ruoff, and L. Shi, Phys. Rev. B 91, 035429 (2015).
64. P. Pavone, K. Karch, O. Schutt, W. Windl, D. Strauch, P. Giannozzi, and S. Baroni, Physical Review B 48, 3156 (1993).
65. I. F. Chang and S. S. Mitra, Physical Review 172, 924 (1968).
66. G. Lucovsky, M. H. Brodsky, and E. Burstein, Physical Review B 2, 3295 (1970).
67. P. Sen and W. Hartmann, Physical Review B, 9(2), 367-380 (1974).\
68. L. Genzel and W. Bauhofer, Zeitschrift für Physik B Condensed Matter volume 25,13-18 (1976).
69. L. Bergman and R.J. Nemanich, Annual Review of Materials Science 26, 551 (1996).

CHAPTER 2

EXPERIMENTAL METHODS

2.1 Time-domain thermoreflectance (TDTR)

2.1.1 Theory and Setup

The main experimental technique used in this dissertation for measurements of thermal transport in materials is time-domain thermoreflectance (TDTR), a well-established ultrafast optical based pump-probe technique [1-5]. Over the past two decades, TDTR has emerged and evolved as a reliable, robust, and versatile technique to measure the thermal properties of a wide range of bulk and thin film materials and their interfaces [6]. TDTR measures thermal properties by measuring the thermoreflectance response, which is reflectance change (ΔR) with temperature (ΔT), using pump and probe beams in two-step measurement. The pump beam deposits a periodic heat flux on the sample surface is a short time (~ 400 fs), which causes a temperature change in the sample which can be correlated with a change in its reflectance. The probe beam, delayed in time relative to pump beam, detects the corresponding temperature change through the reflectance change. The thermoreflectance response, as a function of delay time between the arrival of the pump and probe pulses on the sample surface, is correlated to the thermal transport properties of sample layers and interfaces by analytic solution of the heat diffusion equation based on Fourier's law of heat conduction [1,5].

The sample is usually coated with a thin layer of metal, typically 70-100 nm thick. The metal layer serves two purposes: it converts the photons in the laser pulse into thermal energy over a small distance, and it acts as temperature transducer due to the temperature dependence of its reflectivity. I typically coated samples with an optically thick layer of Al ≈ 80 nm thickness as Al has large a thermoreflectance coefficient, $dR/dT \approx 10^{-4}$, at wavelength of 785 nm [7]. For a

small temperature change, i.e., $\Delta T < 10$ K, the reflectance change can be assumed to be linear with the temperature change of metal surface. The determination of thermal transport properties is typically accomplished by adjusting free parameters in the thermal transport model to obtain the best fit between the model prediction and the experimental data.

The schematic diagram of our TDTR system is shown in Figure 2.1. The pump and probe laser in this system are generated from the pulse train output of a Ti:sapphire laser mode-locked at 80 MHz repetition rate and FWHM of ≈10 nm, pumped by a 532 nm Nd:YVO solid state laser with power of 9.5 W. The Ti:sapphire laser output has a pulse duration of < 400 fs with wavelength tunable between 710-900 nm. The typical wavelength of 785 nm we use has an average power of around 1.2 W. A combination of a half wave plate and optical isolator is used to attenuate the laser power and prevent laser pulse from reflecting into the oscillator.

The attenuated laser beam is split by a polarized beam splitter (PBS) cube into a vertically polarized pump beam and horizontally polarized probe beam. The pump and probe beams are further separated spectrally by using a long-pass filter and a short-pass filter, respectively [2]. The spectral separation of the pump and the probe beam is based on "two-tint approach", to prevent the diffusely scattered pump light from reaching the photodiode using a third filter placed before the photodiode. An ultrasteep long-pass edge filter with edge wavelength at 786.7 nm and steepness of 1.6 nm (SEMROCK, LP02-785RE-25) is used for pump, and an ultrasteep short-pass edge filter with edge wavelength at 778.6 nm and steepness of 3.9 nm (SEMROCK, SP01-785RU-25) is used for probe. The same short-pass-filter is used before the photodiode to block the leaked pump beam.

The pump beam is modulated as a square wave at the frequency (f) of 1−10 MHz by an electro-optic modulator (Conoptics, model 350-160) and a function generator (SRS, DS345). The

probe beam is modulated by a mechanical chopper at 200 Hz (SRS, SR540) to provide double modulation. Both beams co-propagate and are focused by a microscope objective lens onto a sample surface. The arrival time of the pump pulse relative to the probe pulse is adjusted by a linear motorized stage. A fiber ring-light is mounted onto the objective lens to illuminate the sample. The dark-field image of the sample surface and the images of pump and probe beams can be observed by a CCD camera (Pixelink, PL-B952). The reflected probe beam is collected by a Si photodiode detector (Thorlabs, DET10A). The polarizing beam splitter (Newport, 10FC16PB.5) that reflects the pump and the short-pass-filter before the photodiode effectively block the leaked pump signal from reaching the Si photodiode. A non-polarizing beam splitter (Newport, 10BC17MB.2) is used for reflection and transmission of the probe beam.

The output of the photodiode is connected to a resonant filter, which is basically a LC circuit and for which the resonant frequency is the same as the modulation frequency (f). The signal is fed into a preamplifier (SRS, SR445A) for 5x gain, and a low-pass-filter of 30 MHz, which blocks odd harmonics of the modulation frequency. The signal is read by a RF lock-in amplifier (SRS, SR844) synchronized with the modulation frequency. The double modulation scheme, cross polarization of pump and probe beams with polarizing beam splitters and "two-tint" approach effectively removes coherent pickup.

The experimental TDTR data consists of the in-phase and out-of-phase voltages, $V_{in}(t)$ and $V_{out}(t)$ recorded by a Si photodiode and picked up by the double modulation process. The in-phase signal V_{in} represents the surface temperature change because of the pulse heating. The decay rate of V_{in}, which represents the cooling process of sample surface due to heat dissipation, directly relates to the thermal diffusivity of the sample. The out-of-phase V_{out} is mainly due to the modulated continuous heating of the sample at the modulation frequency f [5].

In analysis, the data of normalized ratio, $-V_{in}(t)/V_{out}(t)$, is compared to a diffusive thermal model which is an exact numerical solution of the heat diffusion equation for a multilayer structure in cylindrical coordinates.[1] When the pump beam deposits heat flux, the metal film will thermalize with a few tens of picoseconds, while it may take on the order of 100 ps for phonons in a crystalline substrate to behave diffusively. Therefore, the diffusive modeling is not expected to be valid for delay times less than 100 ps. Parameters needed in the thermal model are the pump modulation frequency f, the repetition rate of the laser τ, thickness of each layer h, their heat capacity C, and thermal conductivity Λ (a symmetric rank 2 tensor), and the $1/e^2$ radius of the laser spot w_0. An interface with thermal conductance G is modeled by a layer with a small thickness h_i (1 nm) and a small thermal conductivity Λ_i, $G = \Lambda_i/h_i$.

Among these parameters, most of them are fixed during the fitting of one measurement, which are either measured independently or taken from the science and engineering literature. The thickness of the metal transducer is typically measured by picosecond acoustic.[8] The thermal conductivity of the transducer layer is derived from Wiedemann- Franz law. Literature values of heat capacity of each layer are used. The laser spot size is typically measured by the signal correlation scanned from spatially offsetting the pump and probe beam, *i.e.*, the so-called beam offset method explained in Section 2.1.1.[9,10] In its basic application for a bulk sample, the thermal conductivity of the sample, Λ, and the thermal conductance, G, of its interface with the metal transducer are derived from the best-fit to the ratio data of $-V_{in}(t)/V_{out}(t)$.

2.1.2 Beam Offset TDTR

The conventional geometry of TDTR can be modified for studying different heat transport properties. Feser *et al.* [9,10] proposed beam-offset TDTR and modified solutions for

TDTR signals by taking account of in-plane anisotropy of materials. The beam-offset TDTR is a powerful technique that can measure in-plane thermal conductivity in any arbitrary orientation [11,12,13]. The conventional TDTR employs a large beam size and a high modulation frequency to ensure one-dimensional heat transport in the through-plane direction. The combination of a smaller beam size ($1/e^2$ beam radius w ≈ 3.2 μm) and a low modulation frequency (f = 1.12 MHz) increases the in-plane thermal diffusion length to be comparable to the beam size, and the TDTR signal is significantly affected by in-plane heat transport [9,10]. The sensitivity of in-plane thermal diffusivity of sample is also increased by using a 70-nm-thick NbV film (typically with a thermal conductivity of ~20 W/m-K) as the metal transducer for the beam-offset TDTR experiments instead of the conventional 100-nm-thick Al film (with a thermal conductivity of ~200 W/m-K) [9,10].

In beam-offset TDTR, the out-of-phase TDTR signal is collected as a function of beam-offset distance between the pump and probe at a fixed negative time delay, −50 ps. The in-phase TDTR signal at time delay of +20 ps at a high modulation frequency (~ 11 MHz) is useful to measure the intensity profile of cross-correlation of the pump and probe pulse. I use the beam offset TDTR to measure the three-dimensional thermal conductivity tensors of 2D materials, as presented in Chapter 3.

2.2 Raman Spectroscopy

Raman spectroscopy allows nondestructive characterization of materials based on their unique structure, symmetry, electronic environment, and bonding characteristics and provide quantitative and qualitative analysis of the individual compounds.[14-16]

Raman spectroscopy measurements are performed using custom-built optical system based on an Acton Insight spectrometer (Princeton Instruments). The excitation wavelength is 488 nm from a Spectra-Physics Cyan laser. The excitation laser is focused by a 20×, N.A.=0.4, objective lens. The laser power on the sample is ≈ 6 mW and the $1/e^2$ intensity radius of the focused laser beam is ≈ 5 μm. The backscattered Raman light is collected through the same objective and dispersed by a 1200 mm^{-1} grating. The spectrometer is calibrated using a Si wafer. The frequency shift of the Raman active optical phonon in Si at room temperature is 520 cm^{-1} [17]. We assume a linear relationship between pixel number and Raman shift. We verified our calibration by measuring Raman scattering by O_2 molecules in the air adjacent to an Al-coated sample. We measure the O_2 stretching vibrational mode frequency as 1555 cm^{-1}, within 0.1% of the expected value of 1556.2 cm^{-1} [18].

The expected measured line-shape of a Raman peak is the convolution of a Lorentzian phonon line-shape with the Gaussian response function of the spectrometer. The convolution of a Lorentzian with a Gaussian is a Voigt profile [19]. An approximation for the relation between the full-width-at-half-maximum (FWHM) widths of the Voigt (f_v), Gaussian (f_G), and Lorentzian (f_L) profiles is given by [20]:

$$f_v \approx 0.535 f_L + \sqrt{0.217 {f_L}^2 + {f_G}^2} \tag{2.1}$$

The FWHM of a Voigt profile fit to experimental data for the Raman peak of Si in our Raman spectrometer is 5.4 cm^{-1}. The Voigt profile can be deconvoluted to find the width of the Gaussian spectrometer response function using the previously determined Lorentzian lineshape of Si. The intrinsic FWHM of the Si Raman line is 2.6 cm^{-1} at room temperature [21, 22]. The Gaussian FWHM due to instrumental broadening alone is 3.9 cm^{-1}.

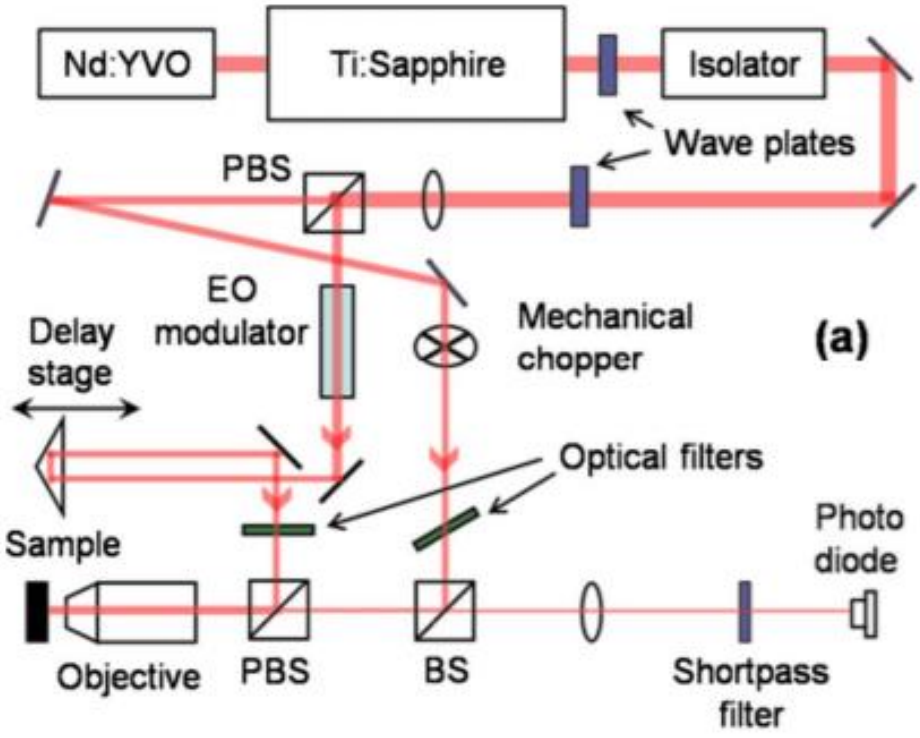

Figure 2.1. Schematic of TDTR system when pump and probe beams are co-aligned and incident on the top surface of a sample [2]. Mode-locked Ti:sapphire pulse laser is split into pump and probe beams, which sequentially heat and measure the change in thermoreflectance of the sample. Optical filters and the short pass filter are used to eliminate the artifacts due to pump beam leaked into the Si photodiode. The sample is sometimes placed on heating stage for temperature dependent measurement as needed.

2.3 References

1. D. G. Cahill, Review of Scientific Instruments 75, 5119 (2004).
2. K. Kang, Y. K. Koh, C. Chiritescu, X. Zheng, and D. G. Cahill, Review of Scientific Instruments 79, 114901 (2008).
3. Y. K. Koh, S. L. Singer, W. Kim, J. M. Zide, H. Lu, D. G. Cahill, A. Majumdar, and A. C. Gossard, Journal of Applied Physics 105, 054303 (2009).
4. S. Huxtable, D. G. Cahill, V. Fauconnier, J. O. White, and Z. Ji-Cheng, Nature materials 3, 298 (2004).
5. P. Jiang, Q. Xian, and R. Yang, Journal of Applied Physics 124, 161103 (2018).
6. D. G. Cahill, P. V Braun, G. Chen, D. R. Clarke, S. Fan, K. E. Goodson, P. Keblinski, W. P. King, G. D. Mahan, A. Majumdar, H. J. Maris, S. R. Phillpot, E. Pop, and L. Shi, *Appl.* Phys. Rev. 1, 11305 (2014).
7. R. B. Wilson, B. A. Apgar, L. W. Martin, and D. G. Cahill, Opt. Express 20, 28829 (2012).
8. G. T. Hohensee, W.-P. Hsieh, M. D. Losego, and D. G. Cahill, Rev. Sci. Instrum. 83, 114902 (2012).
9. J. P. Feser and D. G. Cahill, Rev. Sci. Instrum. 83, 104901 (2012).
10. J. P. Feser, J. Liu, and D. G. Cahill, Rev. Sci. Instrum. 85, 104903 (2014).
11. H. Jang, J. D. Wood, C. R. Ryder, M. C. Hersam, and D. G. Cahill, Advanced Materials 27, 8017 (2015)
12. Y. Zhou, H. Jang, J. M. Woods, Y. Xie, P. Kumaravadivel, G. A. Pan, J. Liu, Y. Liu, D. G. Cahill, and J. J. Cha, Advanced Functional Materials, 27, 1605928 (2017)
13. H. Jang, J. D. Wood, C. R. Ryder, M. C. Hersam, and D. G. Cahill, Advanced Materials, 29, 1700650 (2017).
14. H. H. Willard, *Instrumental Methods of Analysis* (Wadsworth Publishing Company, 1988).
15. P. J. Hendra and P. M. Stratton, Chemical Reviews **69**, 325 (1969).
16. R. S. Das and Y. K. Agrawal, Vibrational Spectroscopy **57**, 163 (2011).
17. K. Uchinokura, T. Sekine, and E. Matsuura, Solid State Communications 11 (1), 47-49 (1972).
18. A. Weber and E. A. McGinnis, Journal of Molecular Spectroscopy 4, 195-200 (1960).
19. D. W. Posener, Australian Journal of Physics 12(2) 184–196 (1959).
20. J. J. Olivero, and R. L. Longbothum, Journal of Quantitative Spectroscopy and Radiative Transfer 17 (2), 233–236 (1977).
21. J. Menendez and M. Cardona, Physical Review B 29(4), 2051 (1984).
22. J. P. Feser *et al.* Journal of Applied Physics 112, 114306 (2012).

CHAPTER 3

THERMAL TRANSPORT IN TWO-DIMENSIONAL MATERIALS WITH IN-PLANE ANISOTROPY

3.1 Sample characterization

The samples for TDTR measurements are prepared by mechanically exfoliating InSe flakes in a controlled atmosphere N_2 glove box using scotch tape on Si(100) wafers covered with a ≈ 1 nm thick native oxide (SiO_x). The exfoliated InSe samples are provided from Prof. Hersam's group at Northwestern University. Each layer of InSe has a hexagonal lattice that consists of two In and two Se close-packed sublayers with the stacking sequence Se–In–In–Se (Figure 3.1a). Thus, each monolayer of InSe consists of 4 covalently bonded sub-layers with an in-plane lattice constant a = 4.084 Å. The out-of-plane lattice constant depends on the specific InSe polytype (e.g., β, ε, or γ), which defines the stacking configuration of the constituent monolayers. For example, the unit cell of β-InSe spans two layers that are rotated by 60 degrees, resulting in a c-axis lattice constant of c = 16.64 Å [1,2,3].

Following exfoliation, the InSe flakes were encapsulated with a ≈ 3 nm thick aluminum oxide (AlO_x) overlayer that provides protection against ambient degradation. In particular, the InSe flakes were first dipped in n-methyl-2-pyrrolidone in the glove box, which results in an organic adlayer that promotes conformal atomic layer deposition (ALD). The AlO_x encapsulation layer was subsequently grown using an established low-temperature ALD protocol without any

---

Parts of this chapter were published in "Anisotropic thermal conductivity of layered indium selenide", A. Rai, V. K. Sangwan, J. T. Gish, M. C. Hersam, D.G. Cahill, *Applied Physics Letters* 118, 073101 (2021).

ambient exposure using an ALD reactor that is directly connected to the glove box [4]. Figure 3.1b shows a representative optical microscopy image of an encapsulated InSe flake.

After encapsulation, the thickness of the exfoliated InSe flakes was measured by tapping mode atomic force microscopy (AFM). InSe flakes with thicknesses ranging from 45 nm to 300 nm and lateral dimensions exceeding 20 × 20 μm^2 were selected for thermal measurements (Figure 3.1b,c). The chemical structure of InSe was confirmed by Raman spectroscopy as shown in Figure 3.1d. β-InSe has D_{6h}^4 point group symmetry, characterized by a hexagonal lattice consisting of eight atoms in the unit cell and extending over two layers (Figure 3.1a). This structure results in three Raman-active vibration modes at ≈ 113 cm^{-1} (A_{1g}^1), ≈ 175.5 cm^{-1} (E_{2g}^1), and ≈ 224 cm^{-1} (A_{1g}^2) as has been previously reported [5-9].

3.2 Through-plane conductivity

The through-plane thermal conductivity of exfoliated InSe flakes encapsulated with AlO_x was measured by conventional pump-probe TDTR, which is presented in Chap. 2. To analyze the data, the in-phase voltage (V_{in}) and out-of-phase voltage (V_{out}) of the measured thermoreflectance signals are monitored, with the ratio calculated using a thermal model [10]. The modeling requires material parameters such as heat capacity (C), thickness (h), interface conductance (G), and thermal conductivity (Λ).

Before performing TDTR measurements, the encapsulated InSe flakes were coated with a 60 nm thick NbV layer using dc magnetron sputtering, which acts as a transducer in the TDTR measurement. As a result, the samples possess at least five chemically distinct layers in the following structure (from the top): NbV/AlO_x/InSe/SiO_x/Si. Since the thicknesses of the AlO_x layer (3 nm) and the SiO_x native oxide layer (1 nm) are at the single nanometer scale, these

layers were treated as part of the NbV/InSe interface conductance G_1 and InSe/Si interface conductance G_{11}, respectively. The thickness of the NbV transducer layer was measured using picosecond acoustics [11], assuming that the speed of sound in the NbV layer is 5.4 nm ps^{-1}. In addition, the volumetric heat capacity of the InSe layer was assumed to be the bulk value of 1.3 J K^{-1} cm^{-3} [12].

The remaining free parameters are the through-plane thermal conductivity of InSe ($\Lambda_{through}$), the thermal conductance of the NbV(metal)/InSe interface (G_1), and the thermal conductance of the InSe/Si(substrate) interface (G_{11}). For highly anisotropic materials, the anisotropy ratio of the in-plane thermal conductivity to the through-plane thermal conductivity should be included in the thermal model, although its effect is significant only at a smaller modulation frequency (f = 1.12 MHz) and a smaller $1/e^2$ beam radius (w ≈ 3.2 μm) [13,14]. This effect can be observed in the sensitivity analysis of TDTR signals ($-V_{in}/V_{out}$) acquired with co-aligned pump and probe beams for different modulation frequencies and beam radii (Figure 3.6d). The sensitivity of the TDTR signal ($-V_{in}/V_{out}$) to a parameter (α) in the thermal model is evaluated using $\partial \log(-V_{in}/V_{out}) \Big/ \partial \log(\alpha)$.

In the TDTR measurements of the through-plane thermal conductivity, a relatively high modulation frequency (f = 11 MHz) and a relatively large $1/e^2$ beam radius of w ≈ 10.6 μm were used, thereby minimizing the sensitivity of the measurement to the in-plane thermal conductivity (Figure 3.6a). In this case, the through-plane analysis is performed iteratively. In particular, the analysis of the data acquired with a co-aligned pump and probe is iterated with the analysis of the beam-offset TDTR signals used to determine the in-plane thermal conductivity until a satisfactory convergence is reached. Example data for a beam-offset TDTR measurement are included in Figure 3.2 and discussed further below. In this manner, the final values for the

components of the thermal conductivity tensor do not depend on the initial guesses. At high modulation frequency and large beam size, the sensitivity of the TDTR signal to the conductance of the InSe/Si(substrate) interface (G_{11}) is also negligible. To determine G_{11}, measurements were conducted using f = 1.12 MHz and w = 3.2 μm, which results in optimal sensitivity as shown in Figure 3.6d.

Figure 3.3a shows that the measured through-plane thermal conductivities are essentially independent of flake thickness (especially, for thicker samples, h > 100 nm) within experimental uncertainty. The measured through-plane conductivity is $\Lambda_{through} \approx 0.76$ W/m-K. The interface conductance between the NbV and the InSe flake is relatively low, $G_1 < 60$ MW m^{-2} K^{-1}, as shown in Figure 3.5, where G_1 is plotted against flake thickness. While this low interface conductance can be partially attributed to the low thermal conductivity of the AlO_x encapsulation layer, it has also been observed previously for interfaces between metals and highly anisotropic layered materials [15-19]. The uncertainty of the measured through-plane thermal conductivity is calculated based on error propagation predominantly from the thickness of the NbV transducer layer. Error propagation from uncertainties in NbV thickness (≈ 5 %) to uncertainties in the through-plane thermal conductivity produces an overall error of ≈ 10 % for the measured through-plane conductivity.

3.3 In-plane conductivity

The in-plane thermal conductivities were measured for InSe flakes with a thickness larger than 100 nm by using a beam-offset method [13,14]. A relatively small spot size of w ≈ 3.2 μm and low modulation frequency (f = 1.1 MHz) were used to optimize sensitivity for the in-plane thermal conductivity. The laser beam intensity has a Gaussian shape, and the TDTR signal as a

function of the relative position of the pump and probe also has a Gaussian shape with a slightly larger width. The full-width-at-half-maximum (FWHM) of the TDTR signal is used in the analysis.

In the beam-offset method, data were collected as the pump beam was translated relative to the probe. The FWHM of the out-of-phase thermoreflectance signal (V_{out}) measured at a negative time delay was used to determine the in-plane thermal conductivity along the direction of the beam offset. Additionally, the width of the in-phase signal (V_{in}) at a small positive time delay and high modulation frequency provides a measure of the spatial correlation of the pump and probe. Figure 3.2 shows an example of a beam-offset TDTR measurement for a 297 nm thick InSe flake at 1.12 MHz. The FWHM of V_{out} at a low modulation frequency of 1.12 MHz and a negative time delay of −50 ps is ≈ 6.22 μm, which is larger than the FWHM of the laser beam profile ≈ 5.32 μm measured at a high modulation frequency of 11 MHz and positive time delay of 55 ps. The in-plane thermal conductivity measurements were restricted to InSe flakes thicker than 100 nm due to the limited sensitivity of the measurement for thinner flakes.

The measured in-plane thermal conductivities are plotted against the flake thickness in Figure 3.4b. The in-plane thermal conductivity is also relatively insensitive to flake thickness within experimental uncertainty. The measured in-plane conductivity is $\Lambda_{in} \approx 8.5$ W/m-K, resulting in a high anisotropy ≈ 11 for the measured in-plane to through-plane conductivity (Figure 3.4). The uncertainty of the derived in-plane thermal conductivity is calculated based on error propagation for the input parameters, predominantly from the uncertainty in the measurement of the FWHM of the TDTR signals and, to a lesser degree, the thickness of the InSe flakes. Specifically, ≈ 5 % uncertainty in the InSe thickness propagates to an uncertainty of ≈ 3 % in the in-plane thermal conductivity.

3.4 Discussion

The through-plane and in-plane thermal conductivity values for exfoliated InSe flakes have been measured using TDTR methods to be 0.76 W/m-K and 8.5 W/m-K, respectively. These ambient TDTR measurements were enabled by a conformal encapsulation layer (3 nm thick ALD AlO_x) that contributes negligibly to the interface thermal conductance. Both the through-plane and in-plane thermal conductivity values were found to be essentially independent of flake thickness in the range considered here (≈ 100 – 350 nm). The extracted in-plane thermal conductivity of InSe is smaller than previously measured 2D semiconductors and semimetals such as MoS_2, WS_2, WSe_2, WTe_2, and ReS_2, all of which possess values in the range of ≈ 20 – 100 W/m-K [15-19], which implies that unique thermal management solutions will likely be required for high-density InSe electronic circuits. In addition, the anisotropy ratio between in-plane and through-plane thermal conductivity is also low for InSe (≈ 11) compared to that for transition metal dichalcogenides (≈ 20 to 100). Although the electron mobility of InSe does show high anisotropy (≈ 500) [20-23], its thermal conductivity anisotropy is comparable to black phosphorus (≈ 10)[16]. Strong inter-layer coupling in InSe is likely to contribute to the reduced anisotropy of InSe compared to ReS_2 (anisotropy >100), which has one of the weakest inter-layer couplings among 2D materials[2,24]. Overall, the quantification of the thermal conductivity of exfoliated InSe will inform ongoing effort to utilize ultrathin InSe in electronic, optoelectronic, and thermoelectric applications.

3.5 Figures

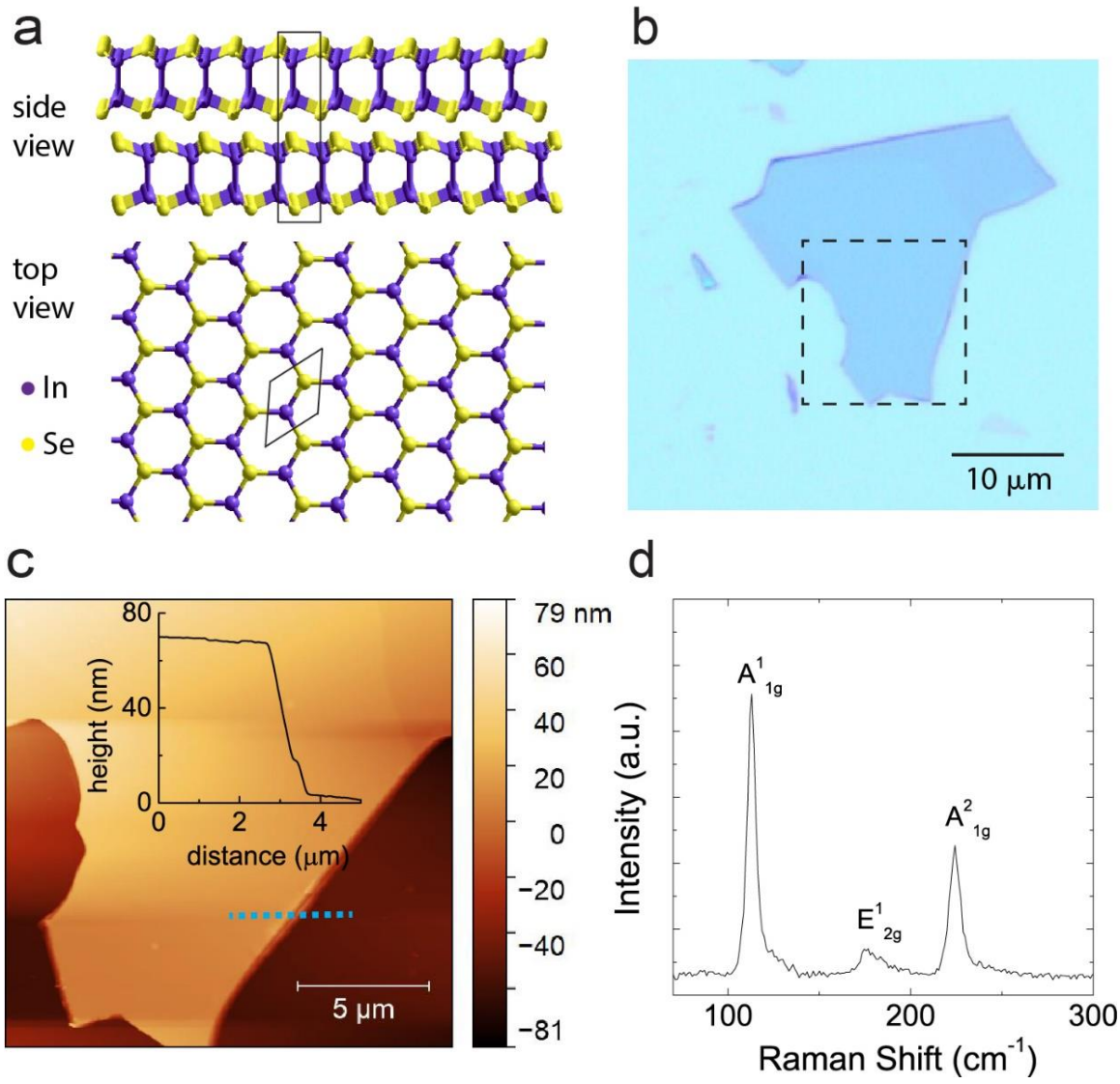

Figure 3.1. (a) Schematic of a β-InSe crystal with a side view and top view. The unit cell spans over two AB stacked layers (rectangle in the side view), while only a monolayer is shown in the top view for clarity. (b) Optical micrograph of an InSe crystal exfoliated on a Si(100) substrate. (c) Atomic force microscopy image of the exfoliated InSe flake encapsulated with 3-nm-thick ALD AlO_x from the region outlined by the dashed line in (b). The inset shows a height profile along the dashed blue line. (d) Raman spectrum of an InSe flake using an excitation wavelength of 532 nm, a 100X objective (NA = 0.9), and a 2400-grooves/mm grating.

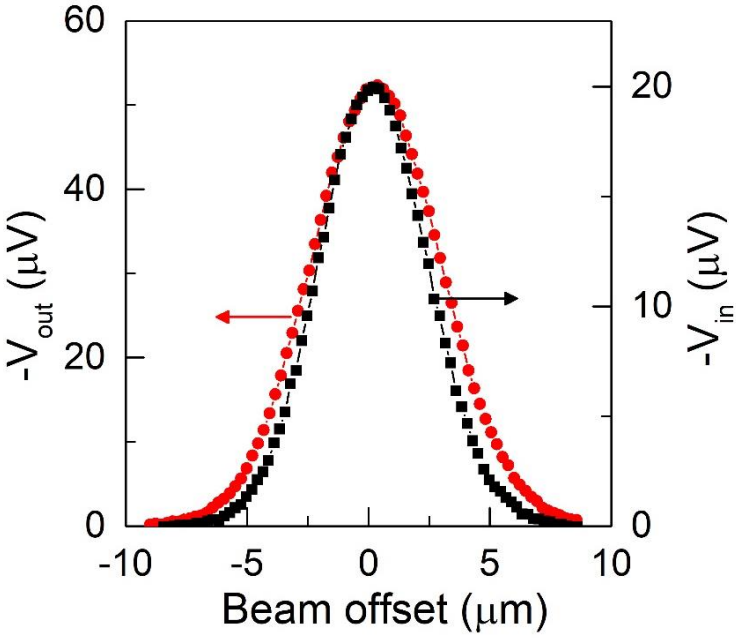

Figure 3.2. In-plane measurements (solid symbols) and the Gaussian fitting curve (solid line) of a 297 nm thick InSe flake (red) at a low modulation frequency of 1.1 MHz and a time delay of 55 ps. The dashed lines show the laser beam profile determined from the in-phase signal at 11 MHz. The $1/e^2$ radius of the pump and probe laser beams is $w \approx 3.2$ μm.

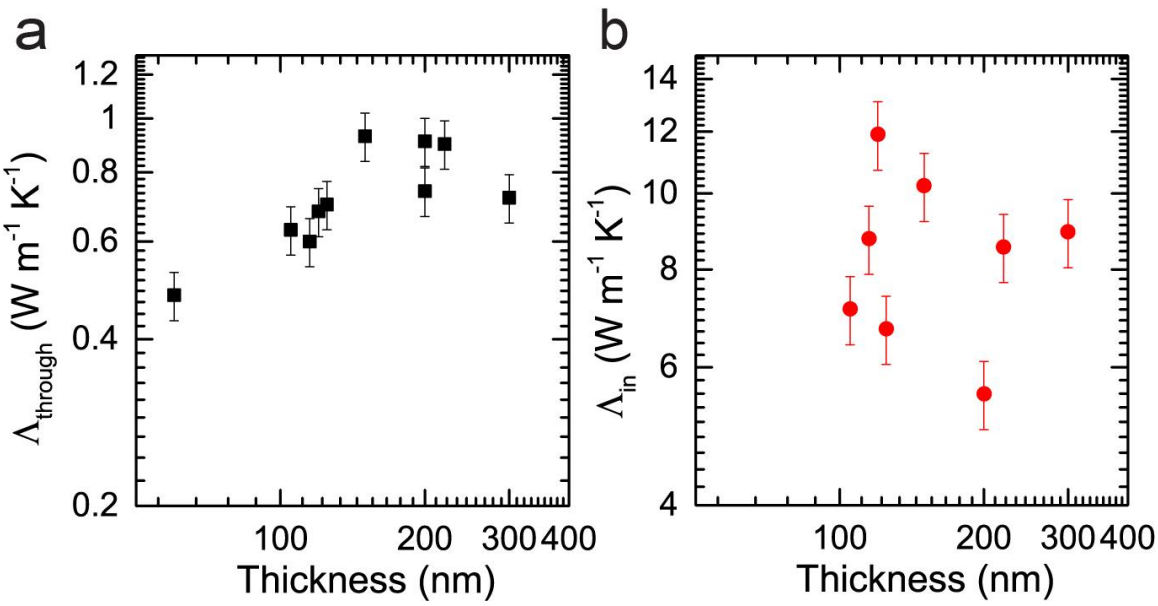

Figure 3.3. Measured (a) in-plane thermal conductivity (Λ_{in}) and (b) through-plane thermal conductivity ($\Lambda_{through}$) of exfoliated InSe flakes plotted as a function of flake thickness.

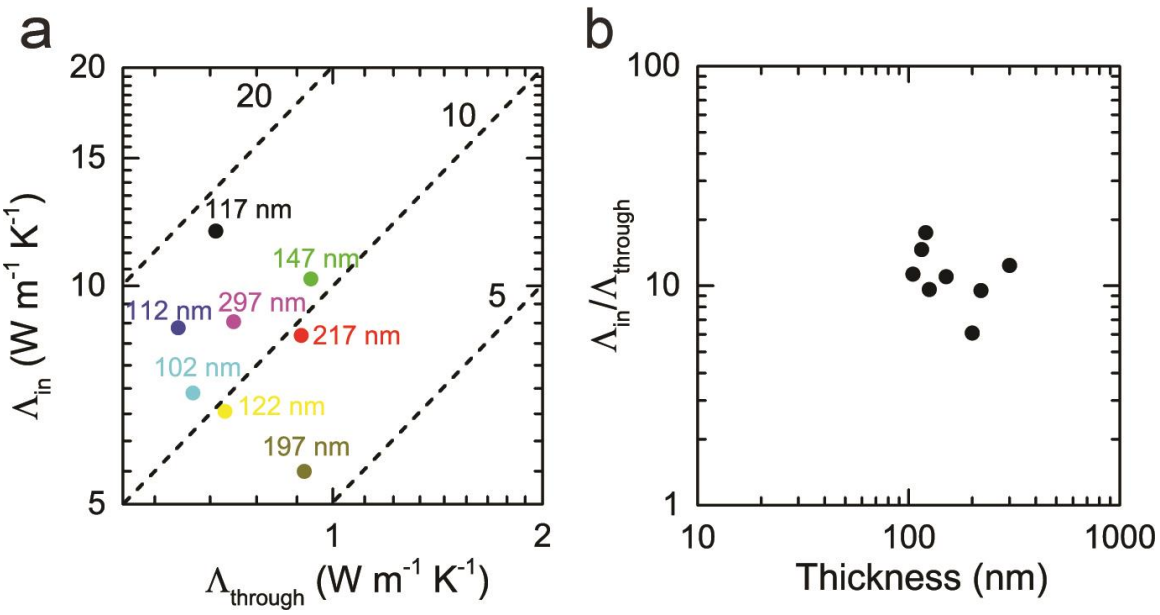

Figure 3.4. (a) Measured in-plane thermal conductivity (Λ_{in}) plotted against the measured through-plane thermal conductivity ($\Lambda_{through}$) for various exfoliated InSe flake thicknesses. (b) The measured anisotropy in thermal conductivity (ratio of Λ_{in} to $\Lambda_{through}$) is plotted as a function of exfoliated InSe flake thickness.

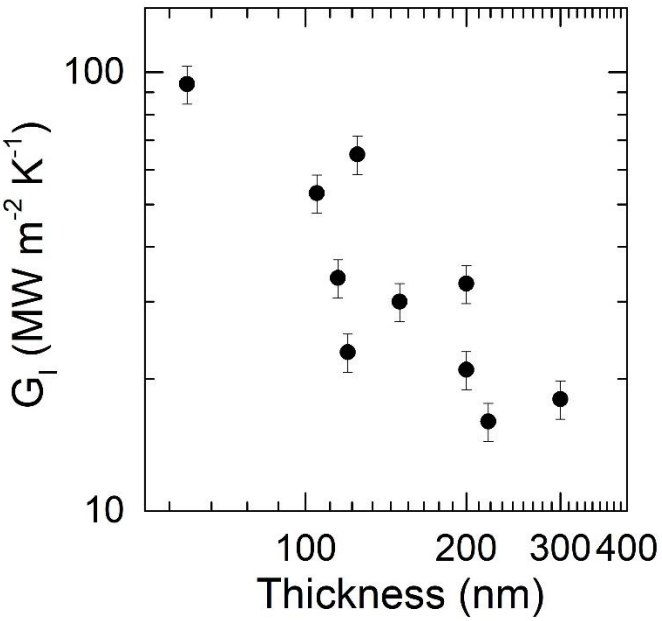

Figure 3.5. Thermal conductance of the metal/InSe interface (G_I) at room temperature as a function of exfoliated InSe flake thickness.

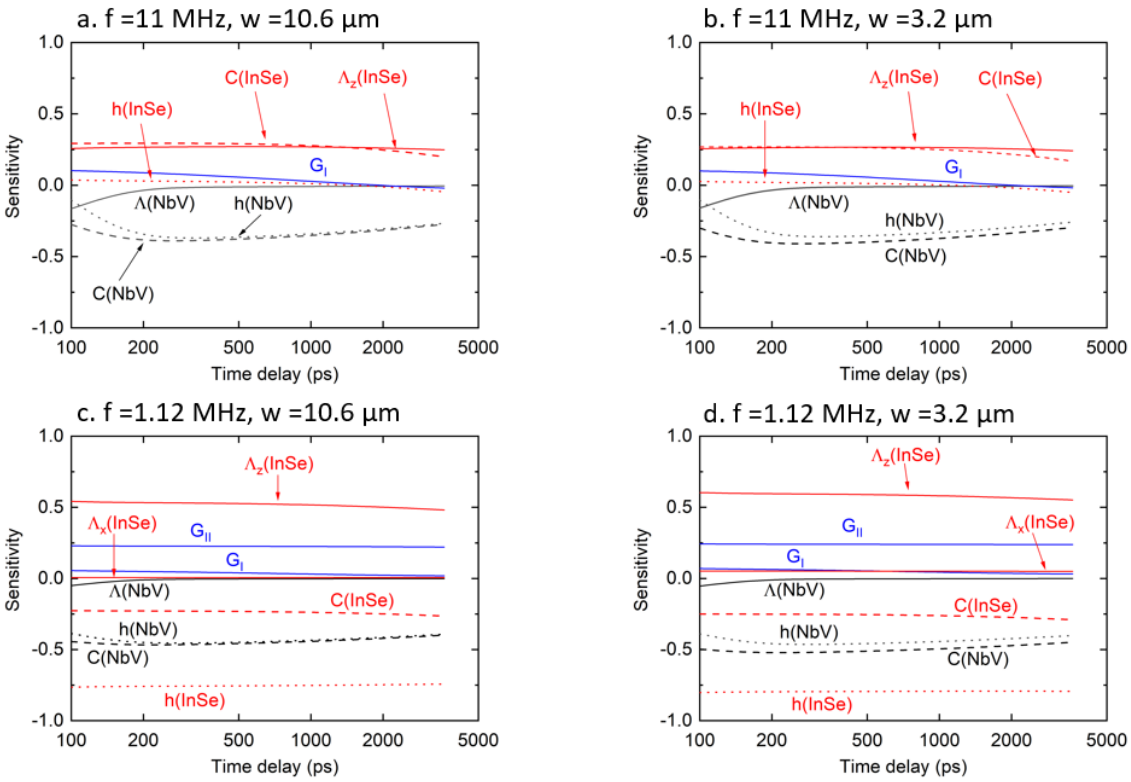

Figure 3.6. Sensitivity analysis of TDTR signals ($-V_{in}/V_{out}$) acquired with co-aligned pump and probe with respect to material parameters of an NbV/InSe/Si specimen at different modulation frequencies (f) and $1/e^2$ beam radii (w). a. f = 11 MHz and w = 10.6 µm, b. f = 11 MHz and w = 3.2 µm, c. f = 1.12 MHz and w = 10.6 µm, and d. f = 1.12 MHz and w = 3.2 µm. NbV and InSe are 60 nm and 147 nm thick, respectively. Λ (solid line), C (dashed line), and h (dotted line) are thermal conductivity, heat capacity, and thickness of the material, respectively. The subscripts in Λ of InSe (i.e., x (solid) and z (solid)) denote the in-plane and through-plane directions, respectively. G_I and G_{II} are the interface thermal conductance of NbV/InSe and InSe/Si, respectively. Sensitivities that are smaller than 0.05 across the full range of time delay and sensitivities are not shown. For these calculations, we set Λ_z (InSe) = 0.93 W/m-K, Λ_x (InSe) = 10.23 W/m-K, G_I = 30 MW m^{-2} K^{-1}, and G_{II} = 20 MW m^{-2} K^{-1}.

3.6 References

1. H. Bergeron, L. M. Guiney, M. E. Beck, C. Zhang, V. K. Sangwan, C. G. Torres-Castanedo, J. T. Gish, R. Rao, D. R. Austin, S. Guo, D. Lam, K. Su, P. T. Brown, N. R. Glavin, B. Maruyama, M. J. Bedzyk, V. P. Dravid, and M. C. Hersam, Appl. Phys. Rev. 7, 041402 (2020).
2. Y. Sun, S. Luo, X.-G. Zhao, K. Biswas, S.-L. Li, and L. Zhang, Nanoscale 10, 7991 (2018).
3. G. Han, Z.-G. Chen, J. Drennan, and J. Zou, Small 10, 2747 (2014).
4. S. A. Wells, A. Henning, J. T. Gish, V. K. Sangwan, L. J. Lauhon, and M. C. Hersam, Nano Lett. 18, 7876 (2018).
5. J. Kang, S. A. Wells, V. K. Sangwan, D. Lam, X. Liu, J. Luxa, Z. Sofer, and M. C. Hersam, Adv. Mater. 30, 1802990 (2018).
6. J. F. Sánchez-Royo, G. Muñoz-Matutano, M. Brotons-Gisbert, J. P. Martínez-Pastor, A. Segura, A. Cantarero, R. Mata, J. Canet-Ferrer, G. Tobias, E. Canadell, J. Marqués-Hueso, and B. D. Gerardot, Nano Res. 7, 1556 (2014).
7. A. Segura, Crystals 8, 206 (2018).
8. S. R. Tamalampudi, R. Sankar, H. Apostoleris, M. A. Almahri, B. Alfakes, A. Al-Hagri, R. Li, A. Gougam, I. Almansouri, M. Chiesa, and J.-Y. Lu, J. Phys. Chem. C 123, 15345 (2019).
9. R. C. Schofield, Ph.D. dissertation, The University of Sheffield, 2018.
10. D. G. Cahill, *Rev. Sci. Instrum.* **75**, 5119 (2004).
11. G. T. Hohensee, W.-P. Hsieh, M. D. Losego, and D. G. Cahill, Rev. Sci. Instrum. 83, 114902 (2012).
12. A. V. Tyurin, K. S. Gavrichev, and V. P. Zlomanov, Inorg. Mater. 43, 921 (2007).
13. J. P. Feser and D. G. Cahill, *Rev. Sci. Instrum.* **83**, 104901 (2012).
14. J. P. Feser, J. Liu, and D. G. Cahill, *Rev. Sci. Instrum.* **85**, 104903 (2014).
15. H. Jang, C. R. Ryder, J. D. Wood, M. C. Hersam, and D. G. Cahill, Adv. Mater. 29, 1700650 (2017).
16. H. Jang, J. D. Wood, C. R. Ryder, M. C. Hersam, and D. G. Cahill, Adv. Mater. 27, 8017 (2015).
17. G. Zhu, J. Liu, Q. Zheng, R. Zhang, D. Li, D. Banerjee, and D. G. Cahill, Nat. Commun. 7, 13211 (2016).
18. P. Jiang, X. Qian, X. Gu, and R. Yang, Adv. Mater. 29, 1701068 (2017).
19. Y. Zhou, H. Jang, J. M. Woods, Y. Xie, P. Kumaravadivel, G. A. Pan, J. Liu, Y. Liu, D. G. Cahill, and J. J. Cha, Adv. Funct. Mater. 27, 1605928 (2017).
20. D. A. Bandurin, A. V. Tyurnina, G. L. Yu, A. Mishchenko, V. Zolyomi, S. V. Morozov, R. K. Kumar, R. V. Gorbachev, Z. R. Kudrynskyi, S. Pezzini, Z. D. Kovalyuk, U. Zeitler, K. S. Novoselov, A. Patane`, L. Eaves, I. V. Grigorieva, V. I. Fal'Ko, A. K. Geim, and Y. Cao, Nat. Nanotechnol. 12, 223 (2017).
21. A. Segura, J. P. Guesdon, J.M. Besson, andA.Chevy, J. Appl. Phys. 54, 876 (1983).
22. C. Zhong, V. K. Sangwan, J. Kang, J. Luxa, Z. Sofer, M. C. Hersam, and E. A. Weiss, J. Phys. Chem. Lett. 10, 493 (2019).
23. V. K. Sangwan, J. Kang, and M. C. Hersam, Appl. Phys. Lett. 115, 243104 (2019).
24. S. Tongay, H. Sahin, C. Ko, A. Luce, W. Fan, K. Liu, J. Zhou, Y.-S. Huang, C.-H. Ho, J. Yan, D. F. Ogletree, S. Aloni, J. Ji, S. Li, J. Li, F. M. Peeters, and J. Wu, Nat. Commun. 5, 3252 (2014).

CHAPTER 4

EFFECT OF ISOTOPIC DISORDER ON THE RAMAN SPECTRA OF CUBIC BORON ARSENIDE

4.1: Sample characterization

The single crystals of isotopically tailored *c*-BAs for Raman measurement are prepared by a modified chemical vapor transport (CVT) method using I_2 as the transport agent [1]. The single crystal *c*-BAs samples are provided from Prof. Lv's group at University of Texas at Dallas. The isotopic composition of the *c*-BAs crystals deviates from the nominal composition likely due to the differences of transfer rate during the CVT process caused by the sizes and morphologies of the ^{10}B and ^{11}B powders and is determined using time-of-flight secondary ion mass spectroscopy (TOF-SIMS). Before measurement, we clean the *c*-BAs single crystals by ultrasonication in ethanol followed by distilled water for 3 min each. We then ion polish a {111} growth facet for 5 min using a GATAN PECS II ion polishing system. The operating parameters of the ion polishing system are an Ar ion energy of 6 keV, ion gun current of 45 μA, and grazing incidence angle of 3°.

4.2 Two-mode behavior in cubic boron arsenide

Figure 4.1 shows the normalized Raman spectra of isotopically tailored cubic boron arsenide single crystals from 650 cm^{-1} to 750 cm^{-1} with ^{11}B-rich (panel (a)) and ^{10}B-rich (panel (b)) compositions. The Raman spectrum for nearly pure ^{11}BAs has a single symmetric peak

---

Parts of this chapter were published in "Effect of isotope disorder on the Raman spectra of cubic boron arsenide", A. Rai, L. Sheng, B. Lv, D.G. Cahill, *Physical Review Materials* 5(1), 013603 (2021).

corresponding to the Raman active longitudinal optical (LO) vibrational mode at zone center. We label the peak that we associate with ^{11}B-related vibrational modes as P1. The Voigt profile fit to P1 for nearly pure ^{11}BAs (x = 0.01), is shown in Figure 4.2(a). After deconvolution by the instrument resolution function, the Lorentzian FWHM of this peak is 1.2 ± 0.2 cm^{-1} corresponding to an optical phonon lifetime of 4.4 ± 0.6 ps [2].

As isotope disorder increases in ^{11}B-rich crystals, see Figure 4.1(a), the P1 peak broadens and a second peak, labelled P2, appears where the phonon density-of-states of ^{11}BAs and ^{10}BAs overlap [3]. In the previous study of natural isotope abundance *c*-BAs by Hadjiev *et al.*, the P2 peak was attributed to localized ^{10}B-related optical modes [3]. A recent study on localization of phonons in mass-disordered alloys have shown that for binary isotopic disorder, light impurities can induce localized modes beyond the bandwidth of the host system [4]. The observed two mode behavior is also consistent with the Chang and Mitra criterion discussed above (Eq. 2) [5].

The Raman spectrum for nearly pure ^{10}BAs crystals has a single symmetric P2 peak (Figure 4.2(d)), corresponding to the Raman active LO optical phonons at zone center. The Voigt profile fit to P2, after deconvolution by the instrumental resolutions, yields a Lorentzian FWHM of 1.5 ± 0.3 cm^{-1}. This linewidth corresponds to an optical phonon lifetime of 3.6 ± 0.5 ps [2]. As x decreases from 0.97 to 0.58, i.e., as ^{11}B is substituted for ^{10}B, the P2 peak broadens and a P1 peak appears. We conclude that the two-mode behavior observed in ^{nat}BAs by Hadjiev *et al.* [3] is observed for all isotopic compositions of c-$^{10}B_x{}^{11}B_{1-x}As$ except the compositions that are nearly isotopically pure, x = 0.01 and x = 0.97.

Figure 4.3 summarizes the positions and widths of peaks P1 and P2 as a function of isotopic composition. Since the LO-TO splitting is smaller than our instrument resolution, at any intermediate compositions x, only two frequencies are observed; one frequency is related to the

optical vibrational modes of the lighter ^{10}B-like vibrations (peak P2), and the other frequency is related to the optical vibrational modes of the heavier ^{11}B-like vibrations (peak P1). The dashed line in Figure 4.3(a) shows the expected mean-field dependence of the optical phonon frequency on the composition through the reduced mass (Eq. 1.1). For a binary compound, the mean field scaling of Raman frequency only strictly holds for the zone center vibrational mode [8]. Nevertheless, the position of peak P1 compares well with the expected mean field scaling with the square root of reduced mass. The position of peak P2, however, does not follow the same trend. The trend in the Raman shift of the peaks P1 and P2 as a function of isotopic composition is reminiscent of the two-mode behavior observed in mixed crystals that satisfy the Chang and Mitra criteria [5].

Within the framework of the weak scattering limit of the coherent potential approximation (CPA), the spectral broadening of the Raman peak of an isotopically disordered crystal is due to the decrease in the phonon lifetime caused by mass disorder; the broadening is expected to increase with the increasing isotopic mass disorder and reach a maximum at $x = 0.5$. Hadjiev *et al*. calculated the disorder-induced broadening within the CPA and found an extremely small broadening of 0.4 cm^{-1} [3]. The Lorentzian FWHM of both peak P1 and P2 is estimated by fitting the data to a symmetric Voigt profile and deconvoluting the Voigt profile with the instrumental resolution function. The Lorentzian FWHM of P1 and P2 derived from this procedure is summarized in Figure 4.3(b). For isotopically disordered *c*-BAs crystals, the observed broadening is nearly two orders of magnitude larger and therefore cannot easily be attributed to changes in optical phonon lifetime that are produced by mass disorder.

Also, the broadening cannot be attributed to anharmonicity. The three-phonon Klemens mechanism [6] is not active in *c*-BAs due to the large gap between the frequency of the highest

frequency acoustic phonons and the low frequency optical phonons.[3] Based on first-principles calculations by Feng *et al*., inclusion of four-phonon scattering reduces the room temperature optical phonon lifetime from 10^4 ps to 40 ps.[7] Thus, major contribution to phonon renormalization effects comes from fourth order anharmonicity, through a decay of T_2 optical phonon into three acoustic phonons (O→3A).[3,8] Hajidev *et al.* employed a model for this decay channel where T_2 optical phonon with frequency (ν_0) decays into three acoustic phonons each with frequency ($\nu_0/3$) and calculated small contribution to spectral broadening of 0.4 cm^{-1}.[3]. Thus, the observed large spectral broadening with increasing isotopic disorder cannot be attributed to the contributions from isotopic mass disorder and anharmonicity alone. Disorder-activated one phonon optical Raman scattering due to mass disorder and concomitant *k*-vector relaxation may contribute significantly to the spectral broadening.

4.3 Disorder activated Raman Scattering

We observe disorder-activated Raman scattering in the one-phonon Raman spectra *c*-BAs where the usual crystal momentum selection rules are partially relaxed and phonon frequencies with a high density of states appear. We plot the low frequency region of the Raman spectra as Figure 4.4(a). In isotopically disordered sample with compositions x = 0.24, 0.36, 0.60 and 0.74, we observe peaks corresponding to TA (L) at 132 cm^{-1}, TA (W) at 218 cm^{-1} and LA (W) at 275 cm^{-1}. The frequencies of the acoustic phonons do not shift significantly with B isotopic composition and therefore we expect these disorder-activated to be independent of isotopic composition. The high density of states at these frequencies are apparent in the phonon density of states calculated by density functional perturbation theory and plotted in Figure 4.4(b). We also

observe a weak peak in the data for all compositions at 394 cm^{-1}, corresponding to two phonon Raman scattering from transverse acoustic phonons with crystal momentum near the X point.

A similar feature is observed in the one-phonon optical Raman spectra of ^{10}B-rich compositions plotted as 4.5(a). We observe peaks that we tentatively attribute to disorder induced one phonon Raman scattering about 50-90 cm^{-1} below the zone center Raman peak. In isotopically disordered sample with compositions x = 0.58, 0.60, 0.75, 0.88 and 0.97, we observe peaks corresponding to ^{10}B-like TO(W) + TO(K) vibrational modes at ≈ 646 cm^{-1}. For the composition x = 0.97 this disordered induced peak is relatively narrow and weak. With increasing isotopic disorder from x = 0.97 to x = 0.58, this peak broadens and becomes stronger in relative intensity as we expect. We do not observe a shift in the frequency of this peak with B isotopic composition and it close to the expected peak in the optical phonon density of states corresponding to TO(W) + TO(K) at 646 cm^{-1} for x = 1.0. This is shown in Figure 4.5(b), where the optical phonon density of states calculated by density functional perturbation theory is plotted against phonon frequency. The experimentally observed shift in wavevector at Γ point of ^{10}B-enriched crystal (x = 0.97) compared to ^{11}B-enriched crystal (x = 0.01) is ≈ 30 cm^{-1}, very close to calculated shift in phonon density of states with the reduced mass of crystal ≈ 32 cm^{-1}.

Finally, we discuss the effects of strong isotopic disorder on the high frequency regime of the Raman spectra that includes Raman scattering by combinations of two optical phonons, see Figure 4.6(a). We compare our Raman scattering data to calculations of the optical phonon density of states in Figure 4.6(b) where we have plotted the p-DOS against twice the phonon frequency. The second order spectra of the ^{11}B-enriched crystal (x = 0.01) shows two-phonon Raman scattering peaks corresponding to contribution from 2TO(K) and 2TO(W) at 1253 cm^{-1}, 2TO(X) at 1267 cm^{-1}, 2TO(L) at 1348 cm^{-1} and 2LO(Γ) at 1405 cm^{-1}. These two-phonon peaks

are less prominent in the ^{10}B-enriched crystal (x = 0.97) due to a larger background in the Raman intensities that we attribute to Raman scattering by free carriers. The experimentally observed wavevector shift at Γ point of ^{10}B-enriched crystal (x = 0.97) compared to ^{11}B-enriched crystal (x = 0.01) is ≈ 52 cm^{-1}, smaller but comparable to the calculated shift in the phonon density of states with the reduced mass of the crystal ≈ 65 cm^{-1}.

Raman scattering productively probes the high energy and high momentum carrying optical phonon modes near Γ point. In ultrahigh thermal conductivity material like *c*-BAs, where anharmonicity is very weak due to dispersion features (e.g., phonon band gap, acoustic bunching [9]), the heat carrying high frequency acoustic phonons are not significantly scattered by the optical phonons at room temperature. While Raman based techniques can be used as a robust tool to study the thermal transport in materials where acoustic phonon lifetime is significantly affected by optical phonons, the anomalous dispersion features of *c*-BAs prohibit a direct connection between the Raman results and thermal conductivity.

4.4 Figures

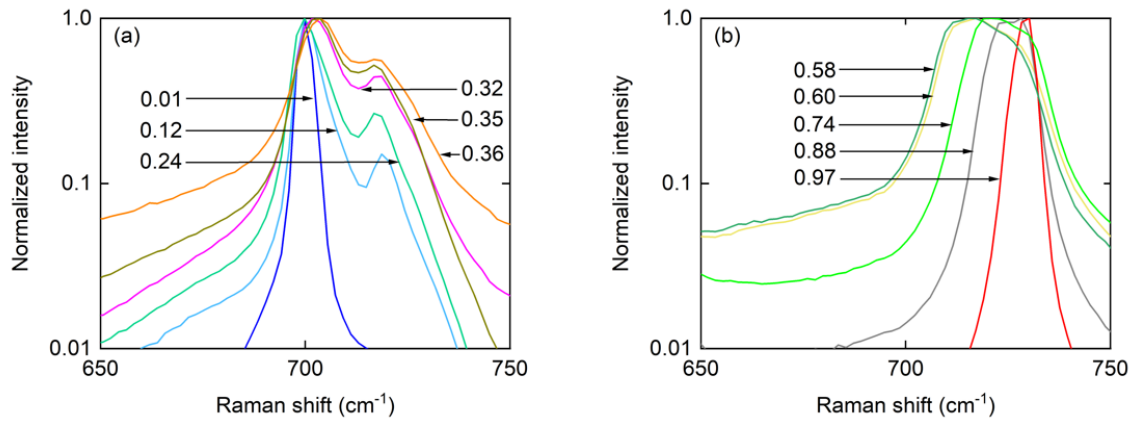

Figure 4.1. Raman spectra of isotopic mixed crystals of c-$^{10}B_x{}^{11}B_{1-x}As$ for (a) $0 < x < 0.4$; and (b) $0.5 < x < 1.0$. The spectra are measured at room temperature with 488 nm laser excitation on {111} growth facets in a backscattering geometry. The measured Raman intensity is normalized by the maximum intensity of the spectrum for each sample. The *y*-axis is logarithmic.

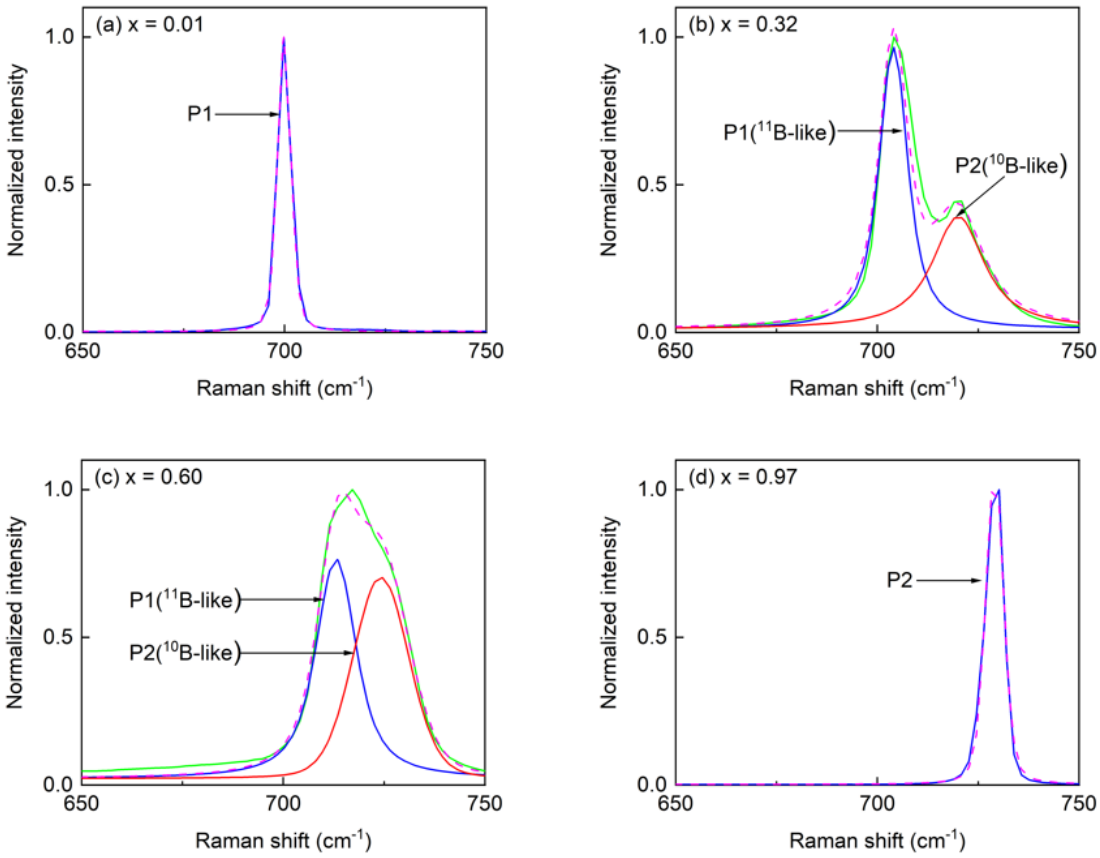

Figure 4.2. The Raman spectra of compositions (a) x = 0.01 (b) x = 0.32 (c) x = 0.60 (d) x = 0.97 are re-plotted. The experimental data are shown as solid lines and fits to a symmetric Voigt profile are shown as dashed lines. The measured spectra are fit to multiple peaks. We attribute peaks P1 (blue) and P2 (red) to ^{11}B-related and ^{10}B-related vibrational modes, respectively.

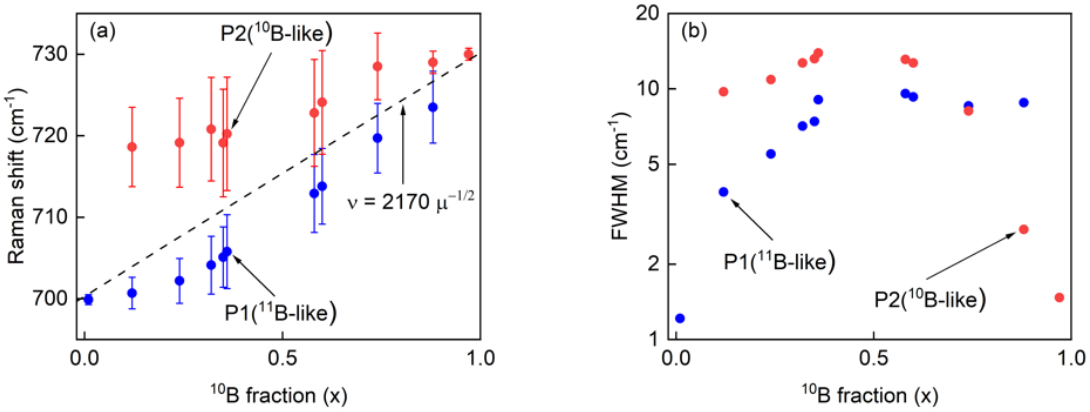

Figure 4.3. (a) The measured Raman shift (ν) corresponding to peaks P1 (blue data points) and P2 (red data points), due to ^{11}B-like and ^{10}B-like optical vibrational modes respectively, with respect to ^{10}B isotopic composition (*x*). The dashed line indicates the expected scaling of the zone center optical phonon frequency with the reduced mass (μ), see Eq. 1. For each isotopic composition, the Lorentzian and Gaussian FWHM of P1 and P2 can be estimated by fitting the experimental data with Voigt profile fit and deconvoluting by the Gaussian instrumental broadening. In panel (a), the Lorentzian FWHM of P1 and P2 are depicted as error bars surrounding the peak Raman shift for each composition. In panel (b), the Lorentzian FWHM of P1 (blue data points) and P2 (red data points) are plotted as a function of ^{10}B composition (x). The y-axis of panel (b) is logarithmic.

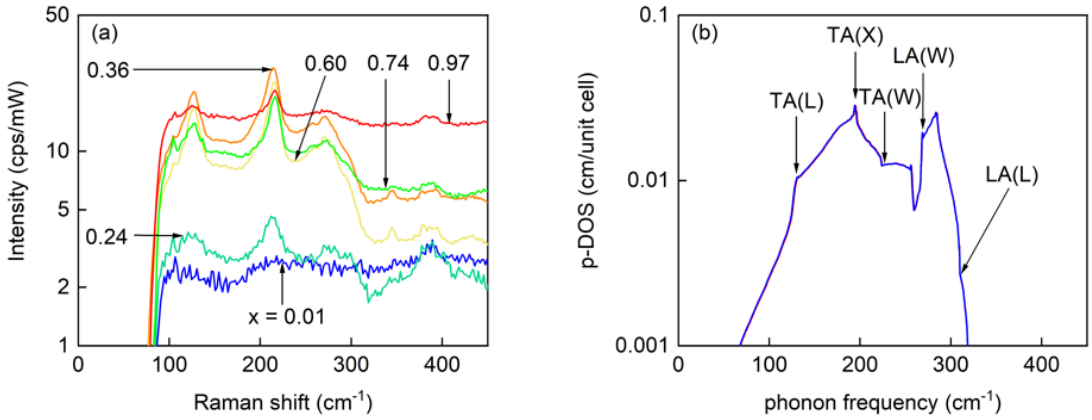

Figure 4.4. (a) Measured Raman spectra of low frequency acoustic phonons in c-$^{10}B_x{}^{11}B_{1-x}As$ for various ^{10}B compositions (x). The intensity in counts per second is normalized by the power of the 488 nm laser excitation in mW units. (b) Calculated phonon density of states (p-DOS) showing critical points associated with transverse acoustic (TA) and longitudinal acoustic (LA) phonons at points on the Brillouin zone boundaries, W, X, and L. Isotopically tailored crystals show disordered induced Raman scattering from acoustic phonons which are not seen in the isotopically enriched crystal (x=0.01 and 0.97). The most prominent features are scattering by the TA phonons at the L and X points. The y-axes of both panels (a) and (b) are logarithmic.

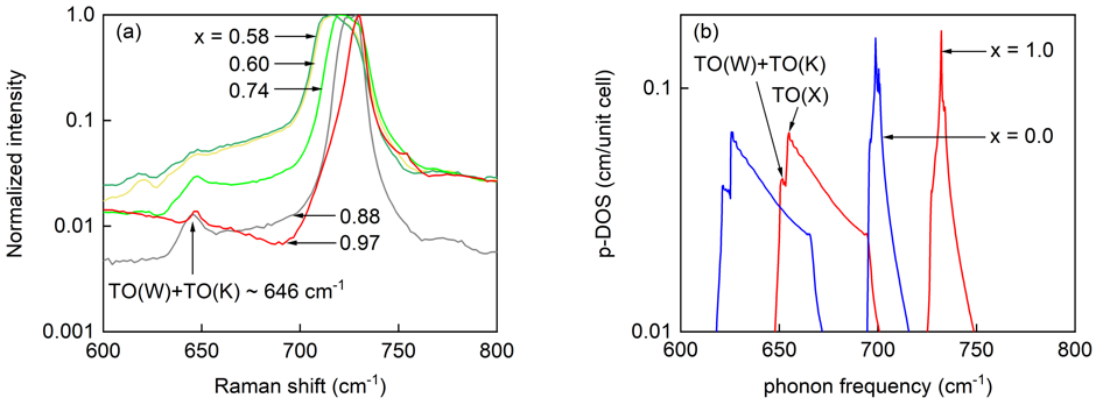

Figure 4.5. (a) Measured Raman spectra of ^{10}B-rich compositions c-$^{10}B_x{}^{11}B_{1-x}As$ in the frequency regime that involves Raman scattering from one optical phonon. The intensity in counts per second is normalized by the power of the 488 nm laser excitation in mW units. Disordered induced excitations for various ^{10}B-rich isotopically disordered crystals can be seen on the low energy tail of the Raman peak corresponding to ^{10}B-like TO(W) +TO(K) vibrational mode at 646 cm^{-1}. (b) Optical phonon density of states (pDOS) calculated by density functional perturbation theory plotted against the phonon frequency to facilitate comparison with the experiment data in panel (a).

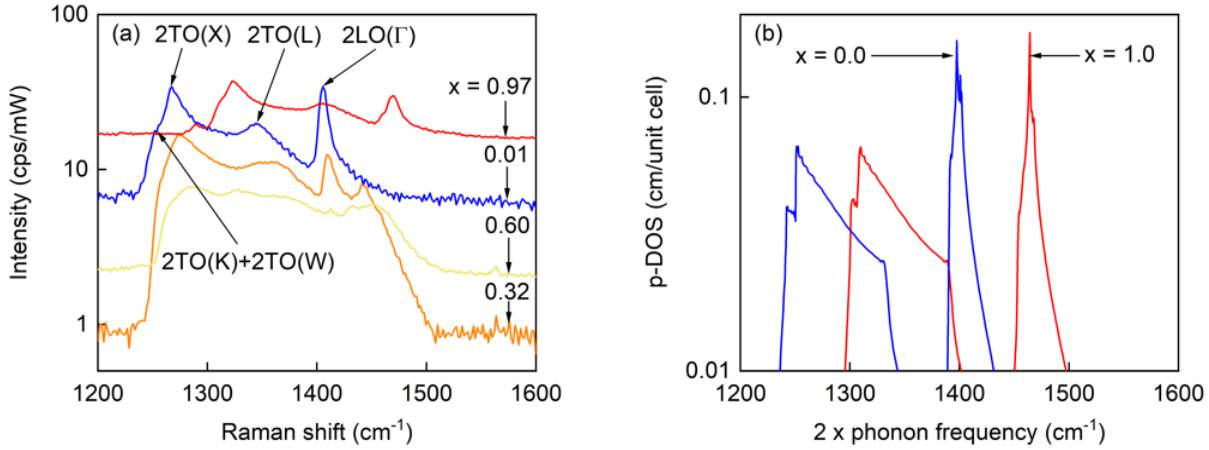

Figure 4.6. (a) Measured Raman spectra in the high frequency regime that involves Raman scattering from combinations of two optical phonons. The intensity in counts per second is normalized by the power of the 488 nm laser excitation in mW units. (b) Optical phonon density of states (pDOS) calculated by density functional perturbation theory plotted against twice the phonon frequency to facilitate comparison with the experiment data in panel (a).

4.5 References

1. S. Li, Q. Zheng, Y. Lv, X. Liu, X. Wang, P. Y. Huang, D. G. Cahill, and B. Lv, Science 361, 579 (2018).
2. J. J. Letcher, K. Kang, D. G. Cahill, and D. D. Dlott, Appl. Phys. Lett., 90, 252104 (2007).
3. V. G. Hadjiev, M. N. Iliev, B. Lv, Z. F. Ren, and C. W. Chu, Phys. Rev. B 89024308, (2014).
4. W. R. Mondal, N. S. Vidhyadhiraja, T. Berlijn, J. Moreno, and M. Jarrell, Phys. Rev. B 96, 014203 (2017).
5. I. F. Chang and S. S. Mitra, Phys. Rev. 172, 924 (1968).
6. P. G. Klemens, Phys. Rev. 148, 845 (1966).
7. T. Feng, L. Lindsay, and X. Ruan, Phys. Rev. B 96, 161201(R) (2017).
8. F. Widulle, T. Ruf, M. Konuma, I. Silier, M. Cardona, W. Kriegseis, and V. Ozhogin, Solid State Commun. 118, 1 (2001).
9. L. Lindsay, D. A. Broido, and T. L. Reinecke, Phys. Rev. Lett. 111, 025901 (2013).

CHAPTER 5

CONCLUSION

In this dissertation, I report the anisotropic thermal conductivities of InSe along the through-plane and in-plane directions at room temperature. The through-plane and in-plane thermal conductivity values for exfoliated InSe flakes have been measured using TDTR methods to be 0.76 W/m-K and 8.5 W/m-K, respectively. The trend of thermal conductivity in 2D materials follows general rules of thermal conductivity: thermal conductivity is higher for the direction of stronger atomic bonding. These ambient TDTR measurements were enabled by a conformal encapsulation layer (3 nm thick ALD AlO_x) that contributes partially to the low interface thermal conductance. Both the through-plane and in-plane thermal conductivity values were found to be essentially independent of flake thickness in the range considered here (≈ 100 – 350 nm). In addition, the anisotropy ratio between in-plane and through-plane thermal conductivity is also low for InSe (≈ 11) compared to that for transition metal dichalcogenides (≈ 20 to 100). The interface conductance between the NbV and the InSe flake is relatively low, G_1 < 60 MW m^{-2} K^{-1} which can be partially attributed to the low thermal conductivity of the AlO_x encapsulation layer. The low thermal conductance along the through-plane direction can seriously limit heat dissipation when 2D materials are implemented in electronic devices. Overall, the quantification of the thermal conductivity of exfoliated InSe will inform ongoing efforts to utilize ultrathin InSe in electronic, optoelectronic, and thermoelectric applications.

Secondly, I studied the effect of isotope disorder on the vibrational spectra of isotopically tailored *c*-BAs single crystals using Raman spectroscopy at room temperature. The two-mode behavior that is predicted by the Chang and Mitra criterion for the substitution of ^{10}BAs in ^{11}BAs is most clearly observed for ^{11}BAs-rich compositions. For ^{10}BAs-rich compositions, the two-

mode behavior is not well developed because the spacing in frequency between the two modes is of the same order as their width. I quantified the Raman wavevector shift in the two peaks corresponding to ^{11}B-like and ^{10}B-like contributions in the Raman spectra and large spectral broadening resulting due to increasing isotopic disorder, anharmonicity and disorder activated Raman scattering. I observed a strong disorder activated one-phonon Raman scattering in the Raman spectra of low frequency acoustic phonons and optical phonons. A similar behavior is seen in high frequency regime of the Raman spectra as well that includes Raman scattering by combinations of two optical phonons.